Article:

Palm, FA, Peakall, J orcid.org/0000-0003-3382-4578, Hodgson, DM orcid.org/0000-0003-3711-635X et al. (5 more authors) (2021) Width variation around submarine channel bends: Implications for sedimentation and channel evolution. Marine Geology, 437. 106504. ISSN 0025-3227

https://doi.org/10.1016/j.margeo.2021.106504

Width variation around submarine channel bends: Implications for sedimentation and channel evolution

Franziska A. Palm[a*], Jeff Peakall[a], David M. Hodgson[a], Tania Marsset[b], Ricardo Silva Jacinto[b], Bernard Dennielou[b], Nathalie Babonneau[c], Tim J. Wright[a]

[a]School of Earth and Environment, University of Leeds, LS2 9JT, UK

[b]Ifremer, Centre de Bretagne, ZI de la Pointe du Diable, CS 10070, 29280 Plouzané, France

[c]Université de Bretagne Occidentale, CNRS, UMR 6538, 29280 Plouzané, France

[*]Corresponding author. E-mail address: franziskapalm@palmlife.de (F.A. Palm).

Highlights

- Width variation around bends in submarine-fan channels is similar to rivers
- Submarine-fan channels are controlled by bank pull (outer bank erosion)
- Bank pull has profound implications for flow and sedimentation processes
- A general wider apex region suggests point-bar development nearer the bend apex
- Width variation is linked to flow characteristics, in turn related to climate

Keywords

Submarine channel, Congo, Channel morphology, Sedimentation, Bank pull, Quaternary, Monsoon, South Atlantic

Abstract

Submarine-fan channels can build the largest sediment accumulations on Earth, but our understanding of flow and sedimentation processes related to channel evolution remains limited. Results from physical and numerical modelling predict dominantly downstream channel bend migration. However, observations and evolutionary models for aggradational submarine channels on passive margins suggest that bends are dominated by lateral expansion. This paradox may be due to limitations induced by the use of constant width channels in process studies. Constant width has been used for two reasons: partly because this is the simplest possible case, but primarily because the width variation around submarine channel bends is unknown. Channel width variations are examined from an active channel reach with 49 bends and three inactive but unfilled channel reaches with a total of 35 bends from the Congo Fan. Each bend was divided into 13 cross-sections, and for each cross-section, channel width was measured for the channel base, and at 10 m vertical increments up to the height of the channel banks. The results indicate that channels are typically wider around bend apices than around inflections. We argue that this morphology suggests that channels are controlled by bank-pull (outer bank erosion), with later deposition at the inner bend, similar to many rivers. The implications of these spatial changes in channel width around bends for sedimentation and channel evolution are explored, and we suggest that such changes may account for the contradictions between physical and numerical modelling, and seafloor observations. Integration of these channel width data with the known climate history of the Congo Fan, further suggests that the magnitude of channel width variation at bend apices may be controlled by allogenic forcing, with larger flows associated with greater width variations around bends.

1. Introduction

Many large submarine-fan channels derive their sediment source from large rivers (e.g. Amazon, Indus, Bengal, Congo and Magdalena). Over time, channels on submarine-fans develop a complex network, which build the largest sediment accumulations on the ocean floor (Flood and Damuth, 1987; Kolla and Coumes, 1987; Curray et al., 2003). Generally, sediment gravity flows enter a network of distributary channels, via a single canyon, of which usually only one channel is active at a time. These flows can interact with the channel by eroding and depositing sediment, before finally depositing sediment as lobes at the end of the channel (Wynn et al., 2007; Prélat et al., 2010; Pickering and Hiscott, 2015). Additionally, the sediment-laden flows can be highly destructive for seabed infrastructure such as seafloor cables and pipelines (Heezen et al., 1964; Carter et al., 2009; Pope et al., 2017). Furthermore, the deposits of submarine channel systems, particularly channel fills and lobes, can form significant hydrocarbon reservoirs (Clark and Pickering, 1996; de Ruig, 2003; Mayall et al., 2006). A better understanding of how channels migrate, and the depositional processes associated, can help improve geohazard assessment, and understanding of the internal architecture of such reservoirs.

During sea level highstand, many submarine-fan channels show reduced activity since most river load is trapped on the inner continental shelf and is not transported to the canyon head (Wetzel, 1993; Burgess and Hovius, 1998; Covault and Graham, 2010). However, a channel on a submarine fan may stay active during highstand (e.g. Burgess and Hovius, 1998; Covault and Graham, 2010), for instance if the canyon is directly connected to the river, as observed for the Congo River (Heezen et al., 1964; Babonneau et al., 2002; Savoye et al., 2009) or through storminduced flows transporting sediment across the shelf and into the channelised system (Kudrass et al., 1998; Guiastrennec-Faugas et al., 2020).

Laboratory experiments and numerical simulations have suggested that submarine channel bends have thinner point-bars relative to channel depth compared to rivers, and these are located further downstream of the bend apex than in fluvial systems (Fig. 1A; Keevil et al., 2007; Peakall et al., 2007; Straub et al., 2008; Amos et al., 2010; Darby and Peakall, 2012; Cossu et al., 2015). These experiments, and simulations, have all used fixed (non-erodible) channel banks. However, in channels with erodible banks the point-bar position would be associated with erosion occurring preferentially at the outer bank, at and beyond the bend apex (Fig. 1A). This imbalance of deposition further downstream of the bend apex and erosion at the outer bend at and beyond the bend apex would lead to downstream bend migration. However, observations and evolutionary models from aggradational channels on passive margins suggest that submarine channels are dominated by lateral bend expansion, and that significant downstream bend migration (more than 2-3 times the channel width) is typically restricted relative to rivers (Peakall et al., 2000a; Deptuck et al., 2007; Jobe et al., 2016); consequently relatively few bend cut-offs form (Peakall et al., 2000a, b). This contradiction between experimental and numerical models, and observations from modern submarine channels, suggests that a key component in the process of sediment deposition around bends is missing. One possible answer to this paradox is that submarine channel bends may exhibit a width variation around bends, similar to that observed in most rivers and incorporated in models (Fig. 1B; Dietrich, 1987; Eke et al., 2014a, b; Duró et al., 2016), rather than the constant channel width which has been used in laboratory experiments and numerical simulations of submarine channels (Imran et al., 1999; Straub et al., 2008; Amos et al., 2010; Sylvester et al., 2011; Ezz and Imran, 2014).

Quantitative analyses of the geometry of submarine channels have been undertaken (Clark et al., 1992; Pirmez and Imran, 2003; Konsoer et al., 2013; Shumaker et al., 2018; Lemay et al., 2020). However, detailed characteristics of cross-sectional morphologies with curvature are rare and typically concentrate on intra-channel deposition and erosion (Babonneau et al., 2004, 2010; Nakajima et al., 2009) rather than on the morphology of the cross-section around bends. Cross-sectional asymmetry around submarine channels increases with curvature, with maximum cross-sectional asymmetry at bend apices (Reimchen et al., 2016), similar to rivers (Knighton, 1982). Such variation of asymmetry around bends further suggests that there is an inter-relationship between flow and morphology. Nonetheless, Reimchen et al. (2016) is a single study from a channel system high on the slope, feeding into a canyon, and it focuses on channel asymmetry. It remains unknown whether there are variations in channel width around submarine channel bends, and if present what the nature of these variations are. Herein, this question is examined using data from the active and several inactive channels on the Congo Fan. In summary, the main aim is to examine the variation of channel width around bends within individual channels, and between channels, which will be addressed by meeting the following objectives: i) to identify appropriate methodologies for measuring channel width in complex submarine channel geometries; ii) to elucidate the variation of width around bends, and compare to results from alluvial rivers; iii) to examine the implications of these variations in channel width around bends in terms of sedimentation and channel evolution; iv) to assess whether submarine channel bends are dominated by bank-pull (outer bank erosion) or bar-push (inner-bend deposition); and, v) to examine the role of climate forcing in controlling variations in width around bends.

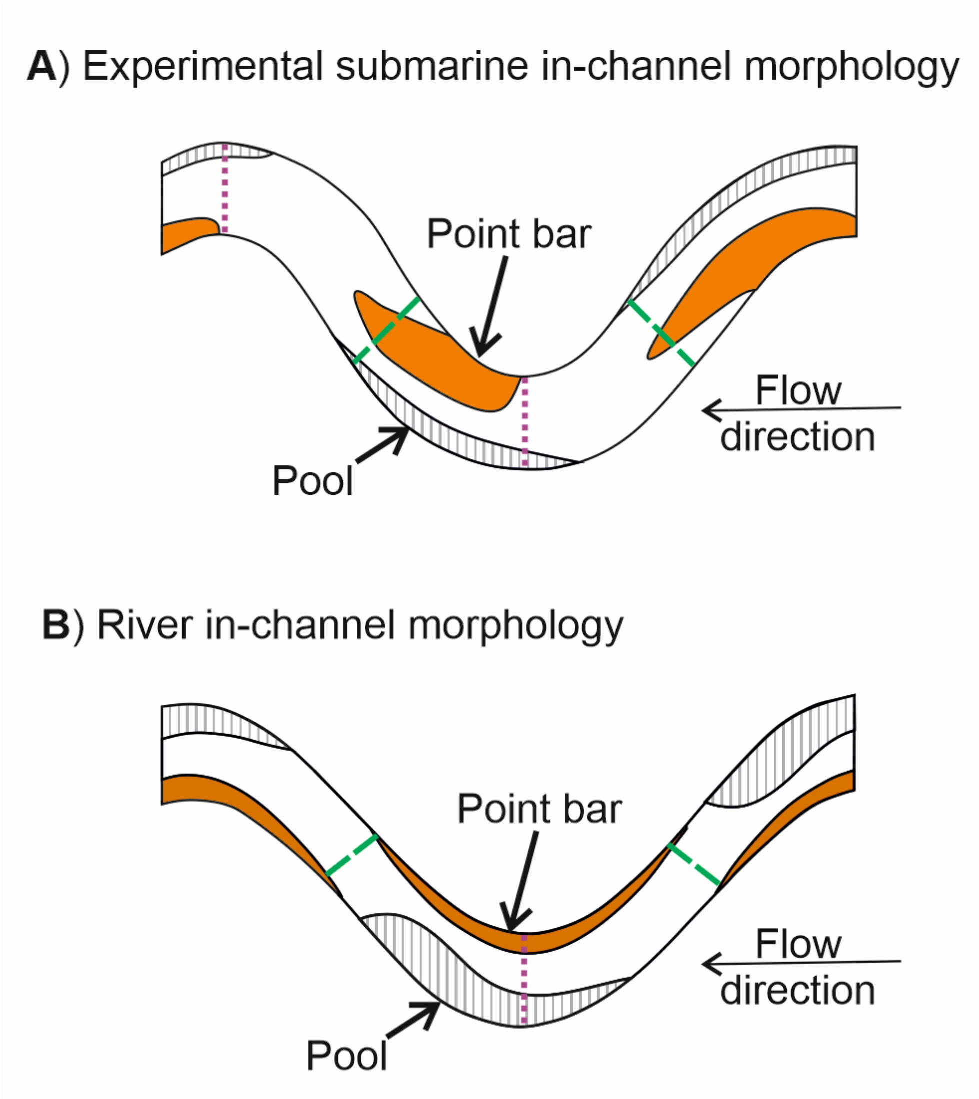

Fig. 1. Schematic diagram of in-channel morphology as a function of bend position and curvature for A) an experimental submarine channel with a constant width, adapted from Peakall et al. (2007) and Amos et al. (2010); and B) a river channel with greater width at the bend apex relative to the inflections, adapted from Trush et al. (2000) and Rossi (2012). Positions of maximum erosion (black stripes) and aggradation (orange area) are shown. Purple dotted lines represent apex cross-section and green dashed lines represent inflection cross-sections. Note that the areas

of enhanced aggradation and erosion are located further downstream relative to the apex in the submarine channel than in the river case.

---

2. Width variations around river bends

Bends in rivers typically exhibit a maximum width at the bend apex, although there is a full range of morphology, including constant width, wider at bend inflection, and channels where bends exhibit no clear pattern (Brice, 1975, 1982; Lagasse et al., 2004; Hooke, 2007). Bends in actively migrating meandering rivers, the 'sinuous point bar rivers' of Brice (1984) exhibit greater widths at bend apices, whereas 'sinuous canaliform rivers' show constant widths (Brice, 1982; Lagasse et al., 2004). Canaliform rivers are marked by greater bank strength as a result of higher clay content or bank vegetation, and consequently they exhibit lower lateral migration rates at bend apices (Brice, 1984; Luchi et al., 2012). Notably, an analysis of 1495 alluvial river bends, demonstrates that over 60% had their maximum width at the bend apex, with a point bar often present (Lagasse et al., 2004). Wider-at-apex channels had a 14% wider width at the bankline from vegetation to vegetation line at the bend apex point compared to mean inflection points (Eke et al., 2014a).

In contrast, a wider-at-inflection width is recognised for many sand-bed and gravel-bed rivers and has been incorporated into the concept of a riffle-pool sequence (Tinkler, 1970; Keller and Melhorn, 1978; Hudson, 2002). Riffle-pool-sequences may occur in a pattern in terms of bend planform with riffle areas occurring at inflection regions and pool areas occurring at apex regions (Tinkler, 1970; Keller and Melhorn, 1978; Hudson, 2002). A variable width or a wider-at-inflection width around bends is often controlled by alternate bar (free bar) formation (Zolezzi et al., 2012; Duró et al., 2016). Alternate bars, or free bars, are bars that develop spontaneously as a result of instability processes and may occur on either side of the bank or as mid-channel bars (Seminara and Tubino, 1989), which causes the channel width to increase at the position of free bars (Zolezzi et al., 2012; Duró et al., 2016).Although the formation and movement of free bars can initiate width changes, ultimately width changes in rivers are controlled by the relative rates of erosion at the outer bank and deposition at the inner bank (Eke et al., 2014a, b).

In rivers, where the variation between the relative rates of erosion and depositionis high, greater width variations occur (Eke et al., 2014a, b). This process of width variation, and in turn bend migration, is therefore controlled by deposition at the inner bend (bar push) or erosion at the outer bank (bank pull), and their relative magnitudes (Nanson and Hickin, 1983; Braudrick et al., 2009; Parker et al., 2011; Eke et al., 2014a, b; Matsubara and Howard, 2014; Van de Lageweg et al., 2014; Wu et al., 2016). Bank pull is related to initial channel widening, and bar push is related to initial channel narrowing (Eke et al., 2014a). Independent results from laboratory experiments and numerical simulations suggest that bend migration of rivers is typically controlled at the bend apex by bank pull through outer bank erosion rather than bar push, for both bed-load and suspended-load deposition (Matsubara and Howard, 2014; Van de Lageweg et al., 2014). However, the observed positive relationship between suspended sediment load and migration rate in certain systems may suggest that bar push dominates in these rivers (Constantine et al., 2014; Donovan et al., 2021).

Constant width, canaliform channels are related to restricted channel banks either through vegetation or silt/clay (Lagasse et al., 2004; Luchi et al., 2012; Matsubara and Howard, 2014); this acts to restrict the bank erosion rate (Luchi et al., 2012), in turn limiting width variation. Some mixed-load and suspended-load alluvial rivers composed of fine sand to silt/clay also have a nearly constant channel width with steep banks (Page et al., 2003; Matsubara and Howard, 2014). Inner bend deposition of these latter mixed-load, and associated suspended-load, rivers consists of oblique accretion deposits, which can form in the absence, or on top of, point bars. Oblique accretion deposits form in a low-energy environment from suspended load and consist of alternating thin sand and mud beds. These beds dip mostly towards the channel. Channel migration is low in these mixed-load and suspended-load rivers but scroll bars and bend cut-offs are formed (Page et al., 2003; Matsubara and Howard, 2014). Hence a constant channel width might be related to a balance between low energy flows and sedimentation, whereby only enough erosion occurs at the outer bank to be balanced by deposition of suspended sediment at the inner bend by secondary flow circulation (Nanson, 1980; Matsubara and Howard, 2014).

3. Geological setting and study area

The Congo Fan is a large active mud-rich submarine fan situated offshore Gabon, Congo and Angola, south of the Gulf of Guinea, on a mature passive margin, reaching a maximum water depth of around 5600 m (Fig. 2; van Weering and van Iperen, 1984; Droz et al., 1996). The fan is composed of at least 100 channel-levee systems from three sub-fans (from north to south: the Northern, Axial, and the Southern Fan) with the Axial Fan (210 ka-present) the youngest sub-fan. Within the sub-fan a single channel-levee system is active at any given time (Droz et al., 2003; Marsset et al., 2009). Abandonment of an active channel is initiated through avulsion (Droz et al., 1996, 2003; Kolla, 2007; Marsset et al., 2009).

The channels on the Axial Fan are chronologically recorded by the avulsion of the feeder channel (Marsset et al., 2009; Picot et al., 2016) and show a total of 52 almost complete channel-levee-lobe systems, called channel-lobes (Ax1-Ax52) by Picot et al. (2016). Four prograding-retrograding architectural cycles were observed from analysis of the channel length and avulsion length, whereby channel length and avulsion length reach a minimum at the end of each cycle: cycle A (Ax01-Ax13), cycle B (Ax14-Ax19), cycle C (Ax20-Ax44), cycle D (Ax45-Ax52), with the current active channel being Ax52 (Picot et al., 2016). The age and timing of each architectural cycle is constrained by dating and/or proxies from cores (Picot et al., 2019). Cycles A and B occurred between 210-70 ka with an average channel duration of 7.4 kyr; cycle C occurred between 70-11 ka with an average channel duration of 2.2 kyr; and cycle D occurred between 11-0 ka with an average 1.4 kyr channel duration (Picot et al., 2019). The 52 channel-lobe systems belong to one of the Northern, Central or Southern Channels, which are independent from the architectural cycles (Marsset et al., 2009; Picot et al., 2016). The Northern Channels with the current active Ax52 channel are the youngest channels on the Axial Fan and follow an E-W orientation. The Southern Channels, which are the oldest channels, follow a NE-SW direction (Picot et al., 2016). The Northern and Southern Channels are separated by a topographic low, where the Central Channels occur. The Ax52 channel is known to be active from frequent cable breaks (Heezen et al., 1964), direct flow measurement (Fig. 2; Khripounoff et al., 2003; Vangriesheim et al., 2009; Azpiroz-Zabala et al., 2017) and recovery of Holocene fine-grained turbidites from cores (van Weering and van Iperen, 1984; Savoye et al., 2009).

The activity of the Ax52 channel is explained by its connection to the canyon and is linked to periods of maximum river discharge (Heezen et al., 1964; Picot et al., 2019). The canyon extends 30 km from the shelf edge into the Congo River Estuary

(Heezen et al., 1964). The architecture and timing of avulsion of the channel-lobe systems on the Axial Fan have been connected to climatic factors controlled by the West African monsoon. During humid periods, river discharge increases and the fan progrades, whilst during arid periods the fan retrogrades (Picot et al., 2019; Laurent et al., 2020).

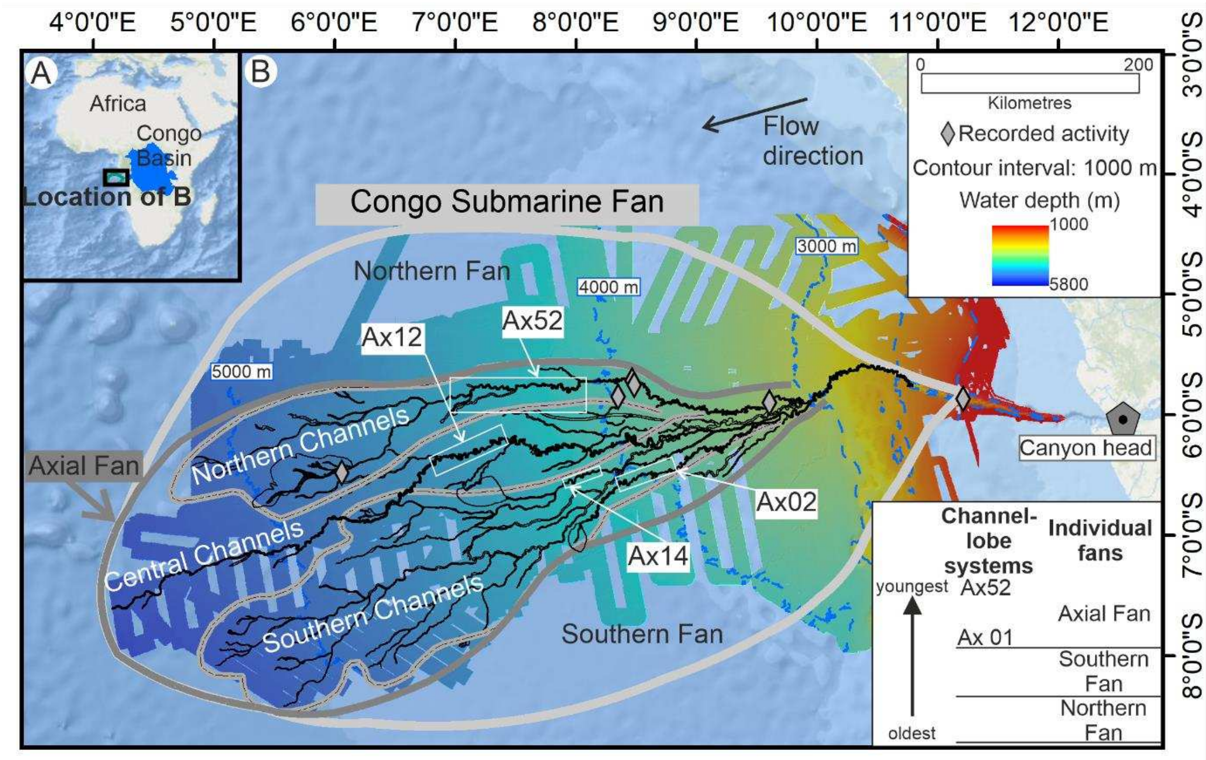

Fig. 2. A) Location of the Congo Submarine Fan and Congo Basin. B) Bathymetry map of the Congo Submarine Fan with its individual fans (Northern, Southern and Axial Fan). The study area is situated on the Axial Fan, the youngest individual fan of the Congo Submarine Fan. The studied channel reaches are part of the Northern (Ax52), Central (Ax12) and Southern Channels (Ax02, Ax14). Channel Ax52 is currently active. The canyon head is the starting point for channel length measurements and is 77 km upstream, as measured by along channel distance, from the point of origin used by Babonneau et al. (2002). Grey diamonds represent positions of recorded activity; data obtained from Khripounoff et al. (2003),

Vangriesheim et al. (2009) and Azpiroz-Zabala et al. (2017). Studied channel reaches are shown as white boxes. Outline of fans, location of channels and relative age of channels are based on Picot et al. (2019).

---

4. Dataset and methodology

Bathymetric maps of the area were constructed during nine scientific cruises between 1992 and 2001 by IFREMER in partnership with TOTAL. Processed EM12 multibeam echo sounder (MBES) data provided a Digital Terrain Model (DTM) with a 100 m horizontal resolution and processed SeaBat7150 MBES data provided a DTM with a 50 m horizontal resolution. Absolute vertical accuracy of the water depth for both DTMs was 0.5% or lower, corresponding to between 10 m for 2000 m water depth and 25 m for 5000 m water depth. ArcGIS 10.3.1 was used to analyse the channels, produce slope maps and to generate cross-sections perpendicular to the channel centreline. Matlab and ImageJ were used to interpret each extracted cross-section and to measure the channel width and height (see Section 4.1).

The channel base was identified as a reference level for each channel because channel bank crestlines can be irregular due to previous mass failure events (Kane and Hodgson, 2011), and crestline heights can vary substantially between inner and outer banks (e.g., up to 80% of mean flow depth, Imran et al., 1999), and spatially around bends, as a result of deposition from super-elevation (Imran et al., 1999). We note that channel bases themselves can be spatially variable as a result of knickpoints of the order of 5-30 m in height (e.g., Vendettuoli et al., 2019; Heijnen et al., 2020; Guiastrennec-Faugas et al., 2021). However, in the observed cross-sections, knickpoints were not observed; if present they are too small to be detected. The channel base is defined as those central parts where the slope approximates to zero, between the points where the lateral gradient abruptly increases. These gradient changes were identified manually using the bathymetry in combination with the slope map of the bathymetric data. The centreline of the channel was determined based on the midpoint of these channel base edges. Note that the centreline is preferred over the thalweg, the deepest part of the channel, as this is simpler to define geometrically and can be measured more accurately. Along the channel base centreline, bends were identified manually between the upstream and dowmstream inflection points (points of minumum curvature) with one bend apex (point of maximum curvature) in between.

Sinuosity, P, defined as the ratio between the distance along the channel, and the straight distance between two points, was calculated for each channel reach and for each bend (Fig. 3A). For bends, sinuosity is given by the channel centreline distance between the upstream and downstream inflection points, divided by the straight-line distance between these two points (Micheli and Larse, 2010). Classifications of straight, low and high sinuosity divisions are variable. The transition between straight and low sinuosity has been taken at: 1.05 (Reimchen et al., 2016); 1.15 (Clark et al., 1992); 1.25 (Babonneau et al., 2010); or, 1.3 (Van den Berg, 1995). Here, the division between straight and low sinuosity was chosen as 1.2, which is an average of all the studies and the same value as Wynn et al. (2007). The transition between low and high sinuosity was defined as 1.5 (Leopold and Wolman, 1960; Clark et al., 1992). Consequently, the following divisions were used: straight ($1 \le P \le 1.2$), low sinuosity ($1.2 < P < 1.5$), high sinuosity ($P \ge 1.5$).

4.1. Methodology for cross-section measurement around bends

Cross-sections perpendicular to the channel base centreline (Figure3B) were taken using the right angle and split tool in the editor of ArcMap, for each bend at a series of positions. For each bend measurements were taken at the apex (7a), inflection points (1ui, 13di), and respectively five equally spaced cross-sections between the upstream inflection point and bend apex (2u-6u), and between the bend apex and downstream inflection point (8d-12d); giving 13 cross-sections for each channel bend. The cross-sections were divided into an inflection region (1ui-3u, 11d-13di; 6 cross-sections) and an apex region (4u-10d; 7 cross-sections, see Fig. 3B).

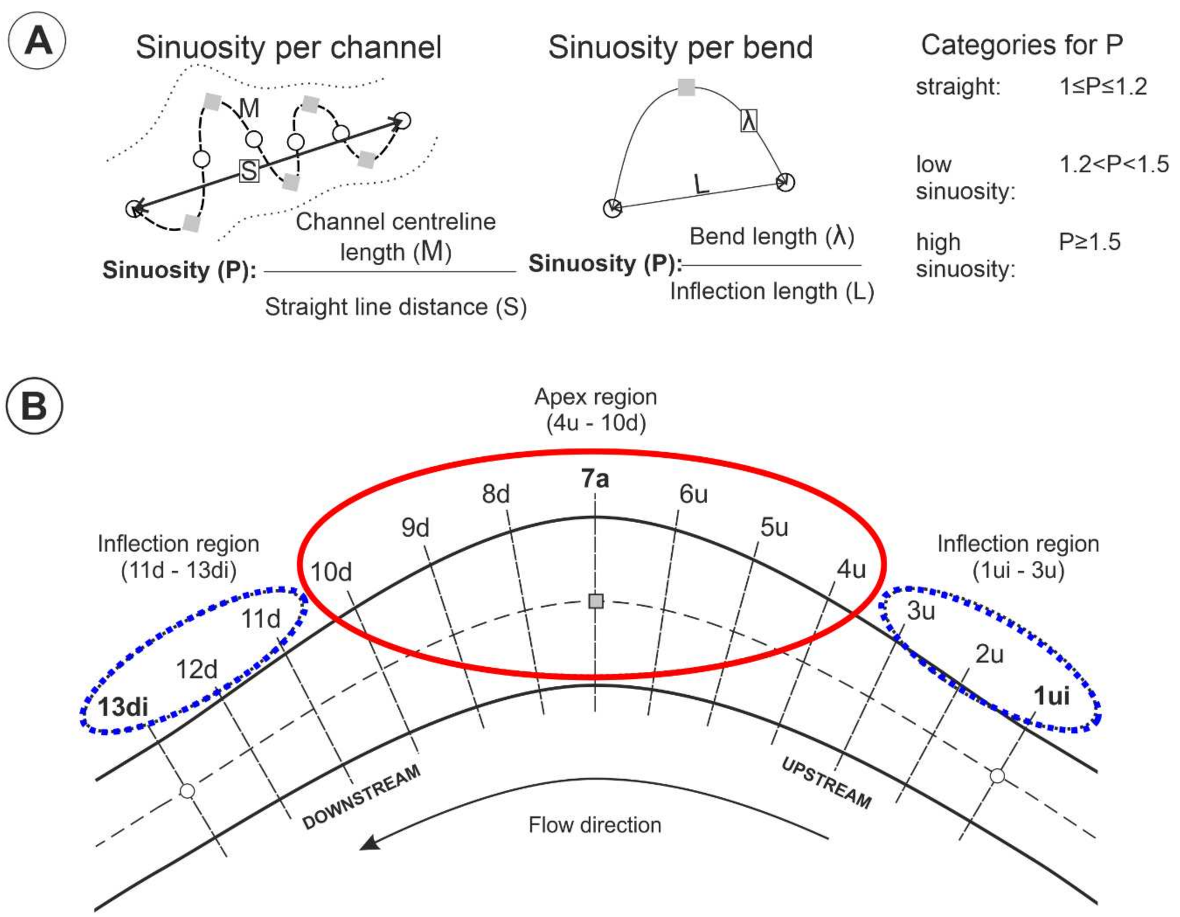

Fig. 3. Methodology for measuring: A) sinuosity, and B) width variation around bends. A) Sinuosity was measured per channel and per bend. B) Methodology for measuring cross-sections around a bend. Flow is from right to left. Thirteen cross-sections per

bend were measured perpendicular to the channel base centreline (dashed line): at the up-stream inflection (1ui, white circle), at the down-stream inflection (13di, white circle), at bend apex (7a, grey square) and 5 cross-sections between the bend apex and up-stream (2u, 3u, 4u, 5u, 6u), and 5 between the bend apex and the down-stream inflection point (8d, 9d, 10d, 11d, 12d). Cross-sections were divided into an inflection region (blue dashed ellipses) and an apex region (red solid ellipse).

For each cross-section of a bend, channel height (H) was measured from the channel base (H_0) centreline up to the outer and inner channel bank crests (H_{Outer} and H_{Inner}, Fig. 4B, C). Similarly, channel width was measured at the channel base (W_0), and at vertical increments (on the channel centreline) of 10 m, up to the outer and inner channel bank crests (W_{outer} and W_{Inner}, Fig. 4B, C). The channel base width was defined as the distance between the points where lateral gradient abruptly increases. These points were identified using the bathymetry in combination with the slope map. It should be noted that this definition of the channel base, may in the case of the inactive channels, incorporate latter stage infill and post-abandonment draping of the channel both of which would act to increase the width relative to that of the original active channel. In a few V-shaped cross-sections that lack a flat floor the channel base width was equivalent to a single point within the resolution of the DTM. In these cases the channel base width was taken as the width of the two adjacent measurement points on the channel cross-section.

For aggradational channels, channel banks are defined between the external levee crests (Kane and Hodgson, 2011; Hansen et al., 2015). The positions of the two channel bank crests on the planform map (Fig. 4A) were identified using a combination of bathymetric and slope maps. For individual cross-sections the bank crests are typically easily identified. In some cases where the crestline position is poorly defined, for instance due to a gentle rise of the banks (e.g., Fig. 4B, inner bend and Fig. 4C, inner bend), planform mapping of crestlines (Fig. 4A) is used to identify the correct position.

Due to the nature of complex topography present within many submarine channels, a cross-section from bank to bank may lead to “erroneous measurements” (Shumaker et al., 2018). Such “erroneous measurements” occur in the Congo channels because of the presence of terraces, which cause the inner bend topography to be lower than the topography at the channel bank crests. These changes to inner bend topography could lead to an overestimation of the channel width due to measuring the channel cross-section twice, either side of the meander neck, and incorrect estimates of maximum channel height (see for example cross-sections D-D’ and E-E’ in Fig. 4D, E). Previous workers have resolved this issue by excluding such erroneous cross-sections (Shumaker et al., 2018). However, we introduce a new methodology that can be used to collect cross-section data from all cross-sections in complex topography. An imaginary bank line is introduced that compensates for the missing topography at inner bend areas with lower elevations; it is here called a trajectory line as it is equivalent to the trajectory line for the migration of scroll bars in rivers (Russell, 2017; Russell et al., 2019). The trajectory line (red dashed lines in Fig. 4) is obtained by connecting the midpoints of opposite cross-sections (1ui and 13di, 2u and 12d, 3u and 11d, 4u and 10d, 5u and 9d, 6u and 8d; see Fig. 3) to the bend apex (7a), and linking this line to the intersection with the inner channel bank crestline. By way of an example, if a terrace was present at the inner bend which would lead to an “unrealistic measurement” (Fig. 4 D, E), channel height and width were measured normally up to the channel crest at the outer bend (e.g. Fig. 4D, E; position D’ of line

D-D’, or position E of line E-E’). However, at the inner-bend, bank-top channel width was measured up to the intersection with the trajectory line (e.g., Fig. 4E, position c1 for line E-E’). In rare cases an exception occurred if the cross-section did not intersect with the trajectory line. In these cases, channel width was measured up the position of the maximum elevation of the inner bend along the cross-section (e.g., Fig. 4D, position b1 for line D-D’). In all cases the corresponding channel height is given as the point where the trajectory line intersects with the channel bank crest at the inner bend (Fig. 4 D, E, position w1 for line D-D’, and position w2 for line E-E’).

In terms of workflow, the cross-sections were extracted from ArcMap using the 3D analyst tool and inserted into Matlab where channel base, bank crests, channel base centreline, and the vertical 10 m increments above the channel base centreline were annotated for each cross-section. Afterwards cross-sections were extracted as an image and loaded into ImageJ where channel height, and channel widths at different height increments were measured.

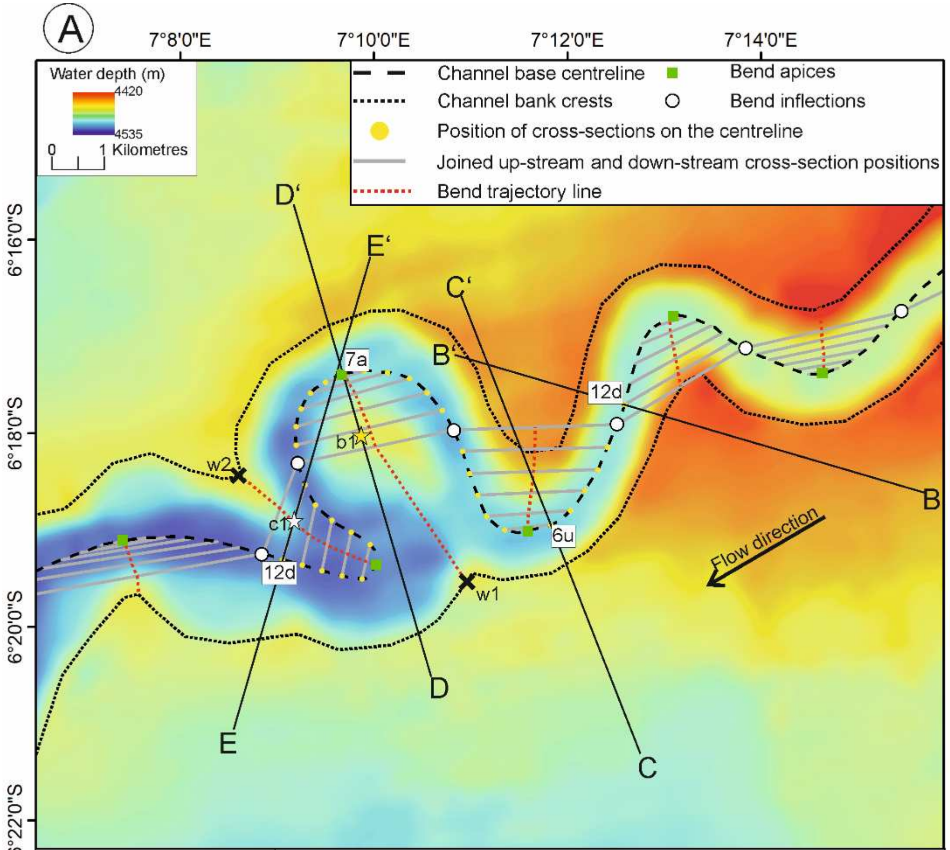

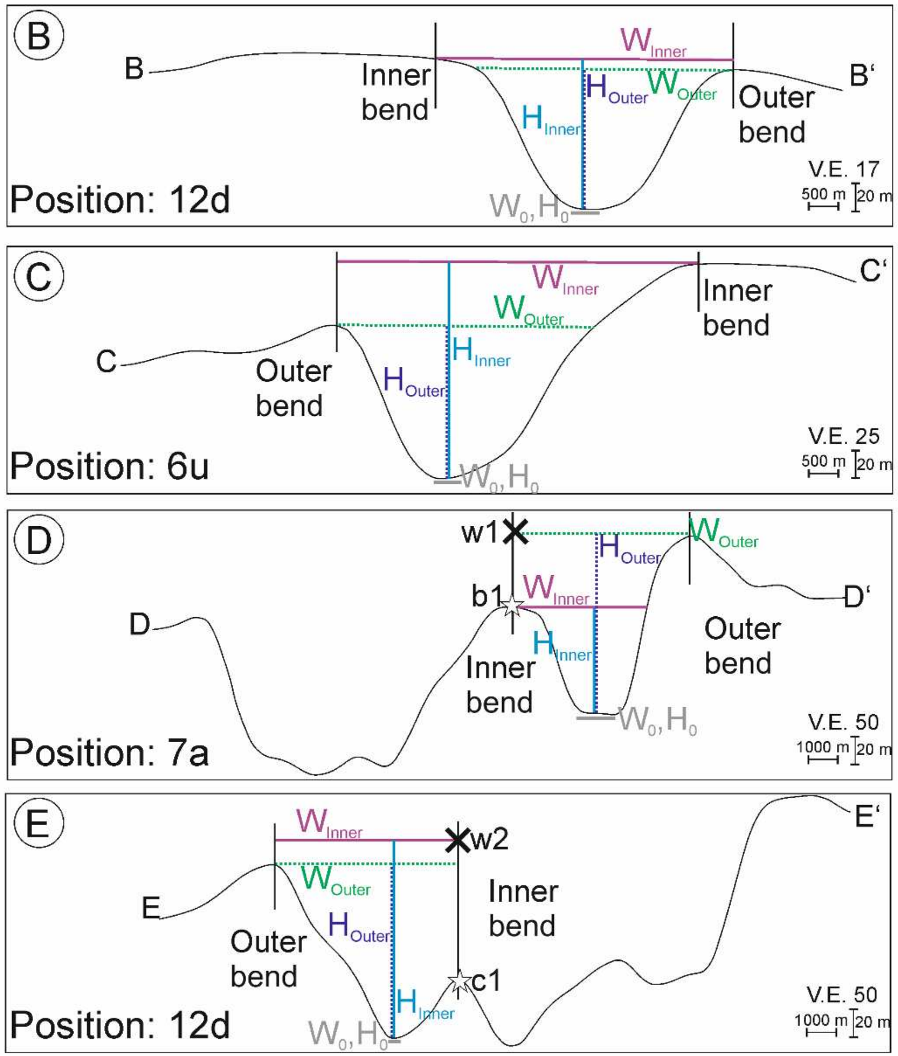

W_0, H_0	Channel base width (W_0), channel base height (H_0=0)
H_{Outer}, H_{Inner}	Height of outer and inner channel bank
W_{Outer}, W_{Inner}	Width at outer and inner channel bank
c1☆	Position of cross-section at bend trajectory line
b1★	Position of cross-section at maximum height at inner bend, no intersection of the cross-section with the bend trajectory line
w1, w2 ✕	Position of water depth measurements at channel bank crest
	Measurements of channel width are taken every 10 m between channel base and channel bank crests

Fig. 4. Methodology for cross-section measurements in submarine channel bends. A) Bathymetric map showing an example of a channel reach with the channel base centreline, channel bank crestlines, bend trajectory lines, and the points on the centreline (yellow dots) where cross-sections would be taken from (see Fig. 3 for details of the cross-sections themselves). For simplicity only 4 channel cross-sections are shown; lines B-B' to E-E'. The grey lines join the centreline points (yellow dots) at equivalent downstream and upstream positions around the bend (e.g., points 6u and 8d, see Fig. 3). Trajectory lines are connected along the mid-points of these grey lines. B-E) Examples of width and height measurements from channel cross-sections. At each perpendicular cross-section width and height were measured as followed: channel width was measured at the channel base (W_0), at the channel banks (W_{Outer}, W_{Inner}), and at height intervals of 10 m between the channel base and channel banks; channel heights were measured between the channel base (H_0=0 m) and channel banks (H_{Outer}, H_{Inner}). B) Simple cross-section close to bend inflection, showing an inner bend without a clear crestal position; crestal position and height are estimated from the planform map of the crestline on part A. C) Simple cross-section close to the bend apex. D) Complex cross-section at the bend apex, where the bank to bank section at the height of the crestline, crosses the channel twice as a result of a lower elevation of the inner bend. Here, atypically, there is no intersection of the cross-section with the trajectory line (red dotted line). In this case the measured inner bend position is the position of the maximum elevation of the inner bank along the cross-section (position b1). The estimated channel height at the inner bend is measured up to the intersection of the trajectory line (red dotted line) with the bank crest (w1). E) Complex cross-section close to the bend inflection, showing multiple crossings of the channel. The intersection of the cross-section with the trajectory line (c1) is used to identify the inner

bend position, and therefore identify the true width (see text for details). The estimated channel height at the inner bend (w2) is calculated as in D. DTM produced by IFREMER Géosciences Marines – ©IFREMER.

4.2. Channel width measurements: definitions and methodology

There are a number of approaches for measuring channel width variation around bends. At the simplest level, and analogous to many measurements in rivers, bank-top channel width can be measured at the bend apex, and compared to the average of the two inflection points (7a, and 1ui, 13di, respectively; see Fig. 3). For each of these 3 cross-section positions, the following parameters are measured:

Bank-top channel width

$$\overline{W_{Bank}} = \frac{(W_{Outer} + W_{Inner})}{2},$$

where W_{Inner} and W_{Outer} are the widths as measured at the height of the inner and outer banks respectively (see Fig. 4 for details).

A second approach is to measure the *depth-averaged channel width* by averaging the width measurements at different heights within the channel, for the bend apex, and for the two inflection points:

$$\overline{x_{7a}} = \frac{1}{n}\sum_{i=0}^{Banks} x_i = \frac{x_0 + x_{10} + x_{20} + \cdots + x_{Inner-1}\, or\ x_{Outer-1} + x_{Banks}}{n}$$

and

$$\overline{x_{1ui,13di}} = \frac{1}{n}\sum_{i=0}^{Banks} x_i = \frac{x_0 + x_{10} + x_{20} + \cdots + x_{Inner-1}\, or\ x_{Outer-1} + x_{Banks}}{n},$$

where x_0 is the position at a height of 0 m, equivalent to the channel base, x_{10} is 10 m above the channel base centreline, $x_{Inner-1}$ or $x_{Outer-1}$ refers to the last position with a 10 m increment from the channel centreline before the positions of the lowermost of the inner channel and outer channel banks, x_{Banks} is the mean position of the two channel banks (x_{Outer}, x_{Inner}) and n is the total number of measurements at all vertical positions for each cross-section.

One additional factor potentially needs to be taken into account when comparing depth-averaged channel width measurements around submarine channel bends is that channel bank height likely varies spatially around bends. Whilst super-elevation of flow in rivers is very small (Leopold, 1982), it can be two orders of magnitude higher in submarine channels (Dorrell et al., 2003), and therefore bank crestlines vary spatially around bends (Imran et al., 1999). This spatial variation in bank heights in submarine channels may lead to a variation in the number of points in the vertical between different cross-sections, potentially influencing comparisons between sections by making those with more points in the vertical look wider than they are. To account for any bias induced by this variation of points a *comparative depth-averaged channel width* is introduced, where the number of points in all cross-sections at 10 m vertical increments from the channel base (thus excluding channel bank positions), is equal to the cross-section with the least vertical increments within a bend, and is calculated:

$$\overline{x_{7a}} = \frac{1}{n}\sum_{i=0}^{x_{max}} x_i = \frac{x_0+x_{10}+x_{20}+\cdots+x_{max}}{n} \text{ and } \overline{x_{1ui,13di}} = \frac{1}{n}\sum_{i=0}^{x_{max}} x_i = \frac{x_0+x_{10}+x_{20}+\cdots+x_{max}}{n}$$

where x_{max} is the height exhibited by the highest 10 m increment in the cross-section with the least number of points in the vertical.

An alternative to only focusing on the bend apex and inflection cross-sections, is to examine width changes around a given bend by using cross-sections from around a bend, and sub-dividing these into the apex region (4u, 5u, 6u, 7a, 8d, 9d, 10d, see Fig. 3 for cross-section nomenclature) and the inflection region (1ui, 2u, 3u, 11d, 12d, 13di). Such an approach has the advantage of synthesising data from the whole bend, and is not reliant on a single cross-section (the apex) or pair (inflections) of cross-sections which may not be fully representative of the broader bend. In particular, studies in rivers have demonstrated that maximum width is often at some point upstream or downstream of the bend apex (Eke et al., 2004a). These aspects, in combination with the greater channel depths and the associated topographic complexity of the Congo channels, relative to rivers, suggest that this approach has potential for providing a broader comparison of bend regions. This approach enables the smoothing of any outliers at apices and inflections, and the capture of maximum width if it is not located at the bend apex. We then examine how these region-based measures compare to those derived from focusing on the individual apex relative to the two inflections. As with the apex and inflection cross-section, the *depth-averaged channel width* for these apex and inflection regions, contain all measurements per cross-section from the channel base to the channel banks:

$$\overline{x_{4u-10d}} = \frac{1}{n}\sum_{i=0}^{Banks} x_i = \frac{x_0+x_{10}+x_{20}+\cdots+x_{Inner-1}\,or\,x_{Outer-1}+x_{Banks}}{n}$$

and

$$\overline{x_{1u\iota-3u,11d-13d\iota}} = \frac{1}{n}\sum_{i=0}^{Banks} x_i = \frac{x_0+x_{10}+x_{20}+\cdots+x_{Inner-1}\,or\,x_{Outer-1}+x_{Banks}}{n}.$$

A *comparative depth-averaged channel width* for these apex and inflection regions is also calculated in the same way as for the individual bend apex and inflection cross-sections:

$$\overline{x_{4u-10d}} = \frac{1}{n}\sum_{i=0}^{x_{max}} x_i = \frac{x_0+x_{10}+x_{20}+\cdots+x_{max}}{n}$$

and

$$\overline{x_{1u\iota-3u,11d-13d\iota}} = \frac{1}{n}\sum_{i=0}^{x_{max}} x_i = \frac{x_0+x_{10}+x_{20}+\cdots+x_{max}}{n}.$$

For each of these definitions of channel width, a comparison is made of the relative increase at the apex (or apex region), relative to the inflections (or inflection region):

$$\%\,width\ increase\ at\ apex\ (or\ apex\ region) = \frac{\bar{W}_A}{(\bar{W}_I/100)} - 100,$$

where $\bar{W}_A$ is the apex (or apex region) width, and $\bar{W}_I$ is the inflection (or inflection region) width.

In order to compare variations in channel width in the vertical between different channel bends, the depth-averaged channel width is utilised. The channel height was normalised since channel height of submarine channels can vary: i) in the downstream direction by a few tens of metres (Klaucke et al., 1997), ii) between different channel systems (Shumaker et al., 2018; Jobe et al., 2020) and iii) between channels from the same system (Straub et al., 2011a; Maier et al., 2013). Each cross-section measurement was normalised by the maximum channel bank height for that cross-section. Thus a normalised height of 0 represents the channel base, and 1 is equivalent to the maximum channel bank height of a cross-section. In order to enable aggregation of different cross-sections across multiple bends, width measurements were taken for each cross-section at each intercept of an increments of 0.1 of the normalised height. Subsequently, the mean width was calculated per normalised channel height increment for the apex and inflection, for both points (apex cross-section vs the two inflection cross-sections) and regions, for all channel reaches.

4.3. Error analysis

In this analysis, a differentiation is made for horizontal errors between the error arising from the DTM resolution, and the standard error of the mean associated with the sampled distributions. The different studied channel reaches have DTMs with either a horizontal resolution of 50 m or 100 m (cell size). The maximum absolute horizontal error for each point, P_i (Fig. 5A), associated with gridding at a given resolution is given by:

$|\delta_{max} P_i| = \sqrt{(25)^2 + (25)^2} = 35.4\ \mathrm{m}$ for the 50 m resolution dataset,

and

$|\delta_{max} P_i| = \sqrt{(50)^2 + (50)^2} = 70.7\ \mathrm{m}$ for the 100 m resolution dataset.

Therefore each width, measured between two points, has a maximum absolute horizontal error of 70.7 m for the 50 m resolution DTM or 141.4 m for the 100 m resolution DTM. The absolute error distribution around a grid point, P_i, on the DTM is shown in Fig. 5B, and the absolute mean is 0.54 of the maximum value, thus 19.1 m or 38.2 m for the 50 m and 100 m DTMs respectively; giving mean absolute width errors of 38.2 m or 76.4 m.

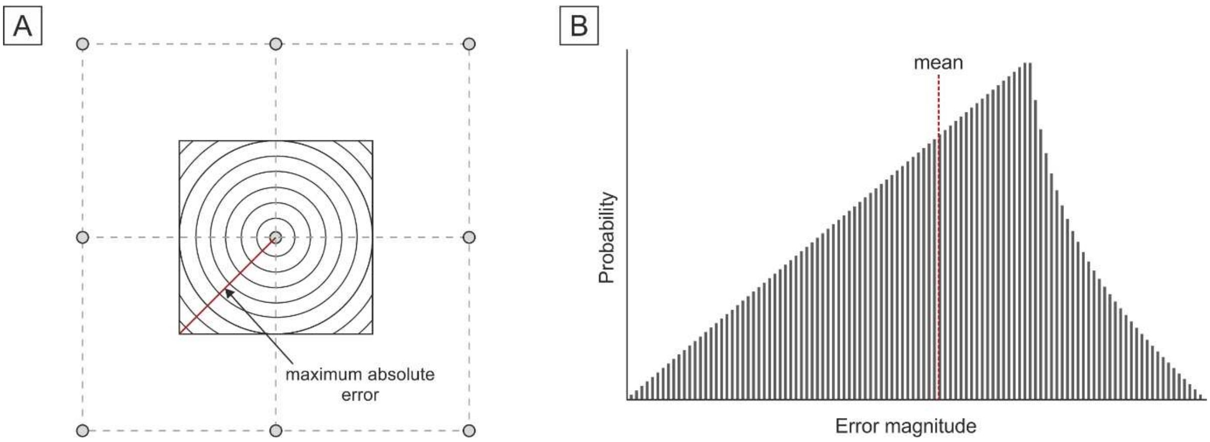

Fig. 5. Absolute error distribution around a point on a DTM grid. A) Planform view of a DTM grid, showing the distribution of distances (errors) around a point; the length of the maximum absolute error is shown with a red line. B) The probability density function of absolute errors around a DTM point; generated from choosing randomly selected points in the unit square and calculating the distance to the centre. The mean absolute value is 0.38 of the cell size (Weisstein, 2021), thus 0.54 of the maximum absolute error.

When taking width measurements from a DTM grid, however, the errors of interest are not absolute values, as there will be both positive and negative errors. With increasing numbers of measurement points the mean error would tend towards zero. Whilst the absolute error distribution for a point, P_i, (Fig. 5B) is not a Gaussian distribution, an approximation of the effect of the number of measurement points can be given by considering the standard error of the mean, $\sigma_{\bar{x}}$:

$$\sigma_{\bar{x}} = \frac{\sigma}{\sqrt{n}},$$

where σ is the standard deviation, and n is the number of measurement points. The best fit Gaussian to the distribution has a standard deviation of 0.20 of the maximum absolute error (0.14 of the cell size), giving values of 7.1 m and 14.2 m for the 50 m and 100 m DTMs respectively. However, as the true distribution is non-Gaussian we conservatively use twice the standard deviation:

$$\sigma_{\bar{x}} = \frac{2\sigma}{\sqrt{n}}$$

n values for mean channel width estimates in this study range from 26 to 780 for the 50 m resolution, and from 54 to 4879 for the 100 m resolution datasets. Considering each end of the width measurement separately, this conservatively gives the standard error of the mean for the location error due to each grid point, P_i, as 0.5-2.8 m, and 0.4-3.9 m for the 50 m and 100 m DTM datasets respectively. Thus taking the standard error of the mean for the points at either end of a width measurement, gives combined width errors of 1-5.6 m and 0.8-7.8 m for the 50 m and 100 m DTM datasets respectively. It is noted that as we are using 2 standard deviations from the mean, actual errors will be considerably lower than those estimated here. Lastly, we note that consideration of a planar surface is the conservative case, and that incorporation of a slope as present in reality, will further reduce the width errors; the error progressively diminishing with increasing slopes.

Whilst it is helpful to understand the magnitude of DTM grid related errors in the horizontal as discussed above, it is noted that the estimates of mean channel width in the present study, include systematic effects from variations in the width measurements themselves reflecting true changes in channel morphology, as well as the associated DTM grid errors we discussed above. Given the comparatively small values of the mean grid errors we do not specifically consider them further. Instead we examine the standard error of the mean of the width distributions, of which the grid error is a component of the observed variation.

The error (*δH*) for a single measurement point arising from the vertical resolution can be calculated using the instrumental error of 0.5% of the water depth, *d*, (Picot et al., 2016):

$$\delta H = d * 0.005$$

Thus the absolute maximum vertical error, $|\delta H_{max}|$, arising from one height measurement (two measurement points) is 1% of water depth and varies between channels from 40-45 m for the water depths in our study (Table 1). Non-maximum vertical errors can be estimated through error propagation:

$$\delta H_{Banks} = \sqrt{(\delta \mathrm{H}_{\mathrm{Base}})^2 + (\delta \mathrm{H}_{\mathrm{Mean\ Bank}})^2}$$

giving an error of 0.7% of water depth (Table 1). However, such an approach to estimating vertical errors is highly misleading since for our study we are not interested in the true depth value for a given point, which has these associated errors, but rather in relative errors between two points in the vertical, which have a high degree of spatial correlation (Calder, 2006, 2007; Czuba et al., 2011). The spatially smooth nature of the extracted cross-sections (e.g., Fig. 4) also demonstrates that relative errors across the DTM are far smaller than those calculated assuming errors from true depths. Thus we demonstrate via the cross-sections that we are able to take width measurements at regular 10 m height increments that reflect the broad morphology of the channel form.

Table 1. Summary of the vertical error for height, for each channel system

Channel name	**Ax02**	**Ax12**	**Ax14**	**Ax52**
Water depth (m)	3909 to 4062	4409 to 4633	4105 to 4252	4170 to 4499
Average water depth (m)	4005	4535	4180	4340
Error (δH) for height measurements (m)	28	33	30	31
Absolute maximum error ($\lvert\delta H_{max}\rvert$) for height measurements (m)	40	45	42	43

Statistical analysis was conducted using the two-sample Student's t-test to test if a significant difference exists between bend apex and bend inflection widths, for a range of different width measurements for each channel. The two-sample Student's t-test is used for two samples with different sizes, that are not paired, and which exhibit an underlying normal distribution. The test analyses whether the two means are significantly different, or they are random. The hypothesis is the same for each tested channel. The null hypothesis is that the apex width is not larger than the inflection width. The alternative hypothesis is that apex width is larger than the inflection width. The null hypothesis is rejected if the p-value is less than 0.05, representing a confidence limit of 95%. As discussed later we find p-values of <0.05 for the overwhelming majority of our width measurements, suggesting that despite the epistemic (systematic variations in channel width spatially) and aleatoric (random grid error) uncertainties discussed above, channel widths are larger at bend apices than at bend inflections.

4.4. Characteristics of studied channel reaches

The four studied channel reaches are situated on the Axial Fan of the Congo Submarine Fan and are part of the following channels which are from oldest to youngest: Ax02, Ax12, Ax14 and Ax52 (Picot et al., 2016, 2019; Fig. 5). Ax52 is the active channel and the others are classified as inactive channel reaches. The characteristics of each analysed channel reach can be seen in Table 1. The chosen channel reach for Ax52 is part of the lower channel-levee complex (Babonneau et al., 2002) and was chosen as the degree of overspill starts to increase rapidly in this morphological region (Savoye et al., 2009). Additionally, channel slope is relatively low and channel width is relatively constant (Babonneau et al., 2002). The inactive channels (Fig. 6A-C) were chosen as they have similarities in planform to the active channel (Fig. 6D), but have different locations on the Axial Fan, and were active at different points of prograding/retrograding cycles (termed architectural cycles; Picot et al. 2016). Additionally, Ax02 and Ax14, are covered by higher resolution bathymetric data (50 m resolution compared to 100 m for Ax52 and Ax12). The Ax02 and Ax12 channels were formed during the first architectural cycle, cycle A, of the Axial fan, whereby Ax02 occurred at the beginning of a prograding period and Ax12 occurred during the peak prograding period of cycle A (Picot et al., 2016). Ax14 occurred during architectural cycle B during a peak retrograding phase.

Table 1. Characteristics of each studied channel reach.

Name of Channel	**Ax02**	**Ax12**	**Ax14**	**Ax52**
Channel activity	Inactive	Inactive	Inactive	Active
Horizontal resolution	50 m	100 m	50 m	100 m
Water depth (m)	3909 to 4062	4409 to 4633	4105 to 4252	4170 to 4499
Along channel distance from canyon head (km)	653	853	694	796
Straight distance of reach (km)	52	73	34	124
Distance along channel centreline (km)	70	117	47	179
Sinuosity	low (1.36)	high (1.6)	low (1.42)	low (1.44)

Channel-reach slope (m/m)	0.002	0.002	0.003	0.002
Number of bends with terraces (Total bends)	7 (19)	16 (27)	12 (13)	17 (49)
Number of apex (A) and inflection (I) region cross-sections	133 A and114 I	189 A and 162 I	91 A and 78 I	343 A and 294 I
Fan development	Beginning of prograding period	Peak of prograding period	Peak of a retrograding period	Prograding period

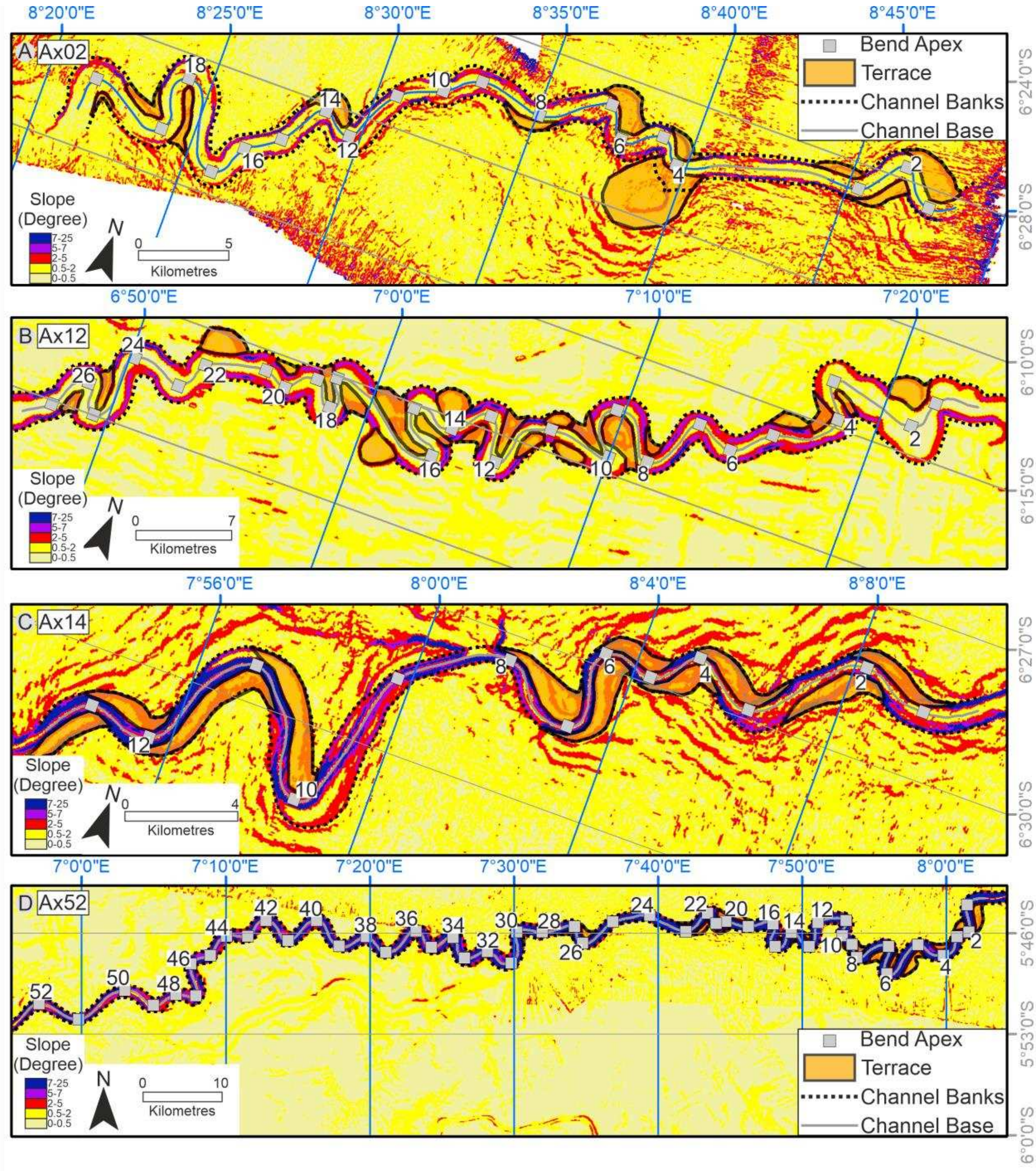

Fig. 6. Slope map with identified terraces and bend apices shown for each studied channel reach. (A) Ax02-channel. (B) Ax12-channel. (C) Ax14-channel. (D) Ax52-channel. Flow direction is from right to left.

5. Results

Here we first examine width variation around bends in individual channel reaches, prior to examining the vertical distribution of channel width, and the relationship between width variations and sinuosity. Subsequently, an analysis of width variations is made for the compound dataset across all four of the channels reaches.

5.1. Variation of channel width around bends in individual channel reaches

5.1.1 Overview

Bank-top channel widths along each channel reach are plotted in Figure 7, and show that the channels vary between ~1 and ~5 km in width, with Ax14 the narrowest channel at ~1-2 km wide, and Ax12 the widest at ~1-4.5 km. The mean bank-top channel width is greater at the apex point compared to the inflection points for the majority of bends in all channel reaches, with 18 of 19 bends (95%) for Ax02 (Fig. 7A), 20 of 27 (74%) for Ax12 (Fig. 7B), 10 of 13 (77%) bends for Ax14 (Fig. 7C), and 31 of 49 (63%) bends for Ax52 (Fig. 7D) wider at the apex point. Most bends (15 of 19 bends) for Ax02 were at least 5% wider at the apex point compared to the inflection points with 6 bends (Fig. 7A) more than 25% wider, and 2 bends greater than 50% wider. Similarly, most bends (19 of 27 bends) for Ax12 were at least 10% wider at the apex point compared to the inflection points, with 8 bends (Fig. 7B) more than 50% wider. In contrast, 6 of 13 bends in Ax14 were more than 10% wider at the bend apex point, with 2 bends >40% wider (Fig. 7C). For Ax52 there were 18 bends more than 10% wider, and 7 bends more than 40% wider. Almost identical results are observed when examining the data in terms of apex regions versus inflection regions (see Supplementary Fig. S1).

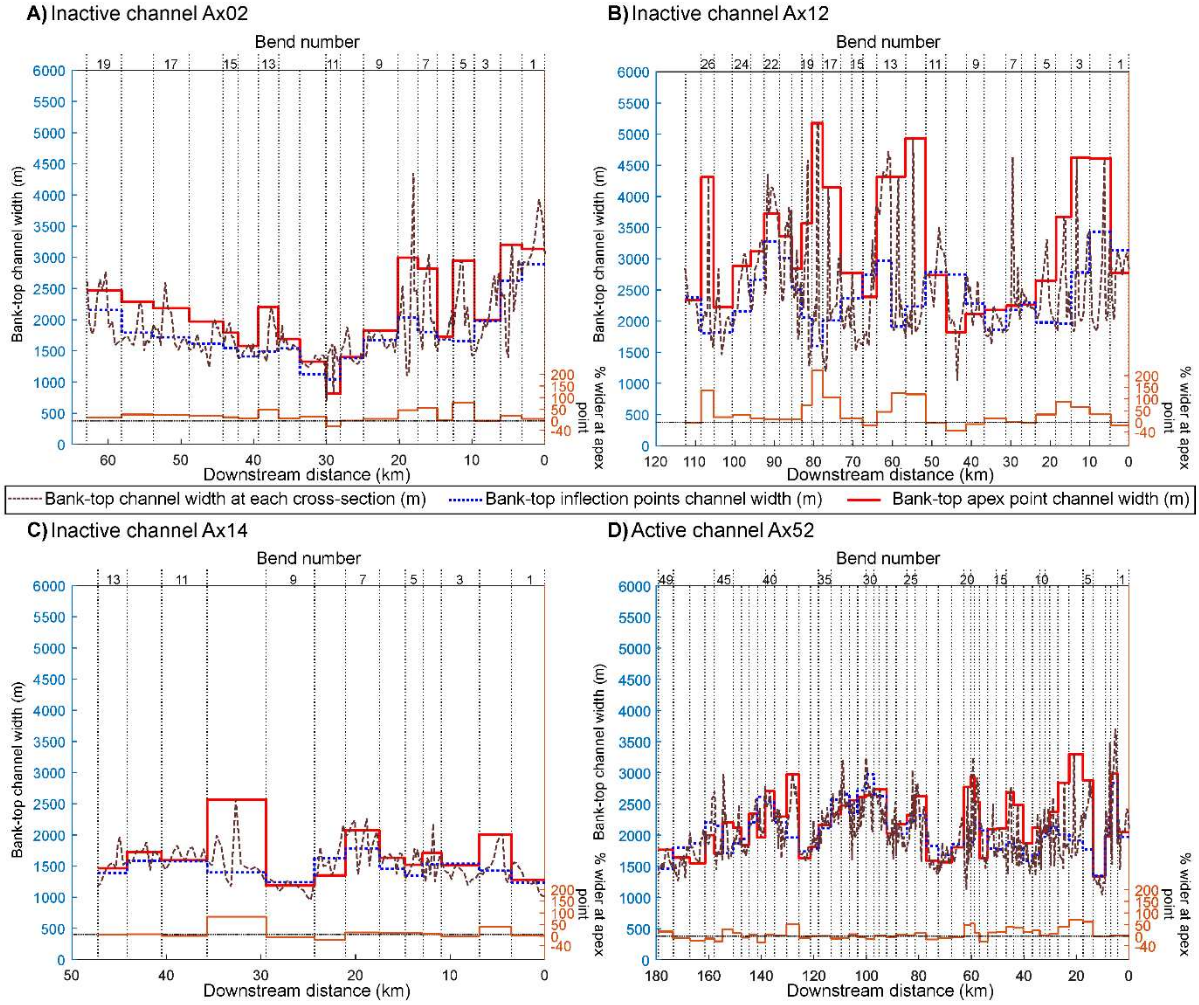

Fig. 7. Bank-top channel width at individual cross-sections (brown dashed-pointed line), at mean bank inflection points (blue dotted line), at bank apex point per bend (red solid line), and % wider at apex point, against downstream distance (km) and bend number for individual channel reaches A) Ax02, B) Ax12, C) Ax14 and D) Ax52. Flow direction is from right to left.

5.1.2 Variation of channel width around bends: bend apex relative to bend inflection points

The simplest measure of width variation around bends, is to compare the bend apex cross-section to the two bend inflection cross-sections. Examining the variation in terms of the bank-top channel width it is observed that the width is wider at the apex point than at the inflection points for all submarine channels (Ax02, 22% or 379 m wider; Ax12, 36% or 856 m wider; Ax14, 13% or 193 m wider; Ax52, 9% or 177 m wider; Fig. 8). These differences between bank-top channel widths around bends are all statistically significant ($p<0.05$; Table 3).

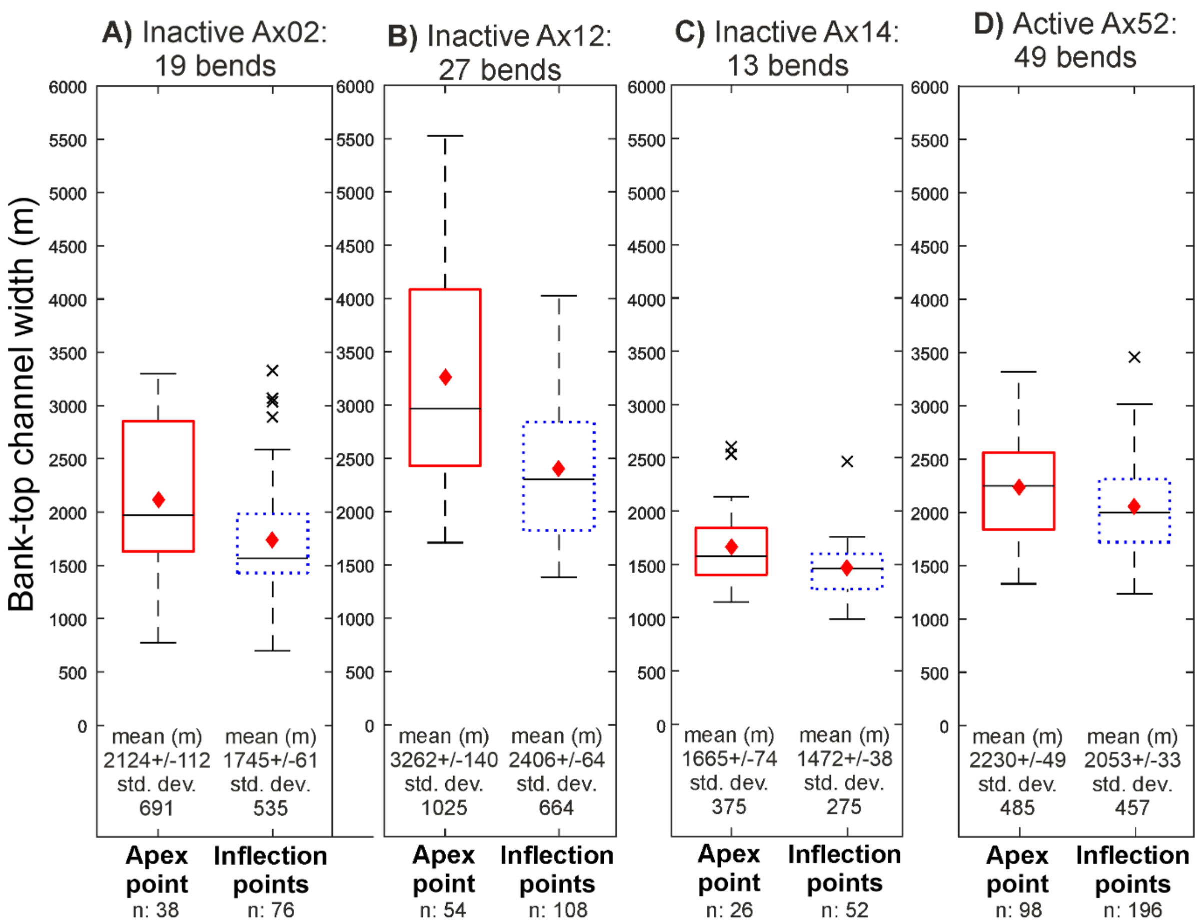

Fig. 8. Box and whisker plots of the bank-top channel width between apex point (7a, red solid line) and inflection points (1ui, 13di, blue dotted line) for A) Ax02, B) Ax12, C) Ax14 and D) Ax52. Data include the widths as measured at the height of the inner

and outer banks. Box indicates 25th and 75th percentiles, “red diamond” indicates the mean, “-” within the box indicates the median, whiskers indicate 99.3% in a normal distribution and “x” indicate outliers. Mean ± standard error of the mean, standard deviation (std. dev.) and the number of measurements (n) are shown for each position.

Looking at depth-averaged measures of the variation between bend axis width and bend inflection width, we assess the mean comparative depth-average channel width (equal points in the vertical), and the depth-averaged channel width (all points in the vertical); see Section 4.2. The mean comparative depth-average channel width is also wider at the apex point than at the inflection points for all submarine channels (Ax02, 22% or 234 m wider; Ax12, 38% or 548 m wider; Ax14, 6% or 35 m wider; Ax52, 8% or 69 m wider; Fig. 9). All of these variations in channel width are statistically significant ($p < 0.05$) except for the narrowest channel Ax14 (Table 3).

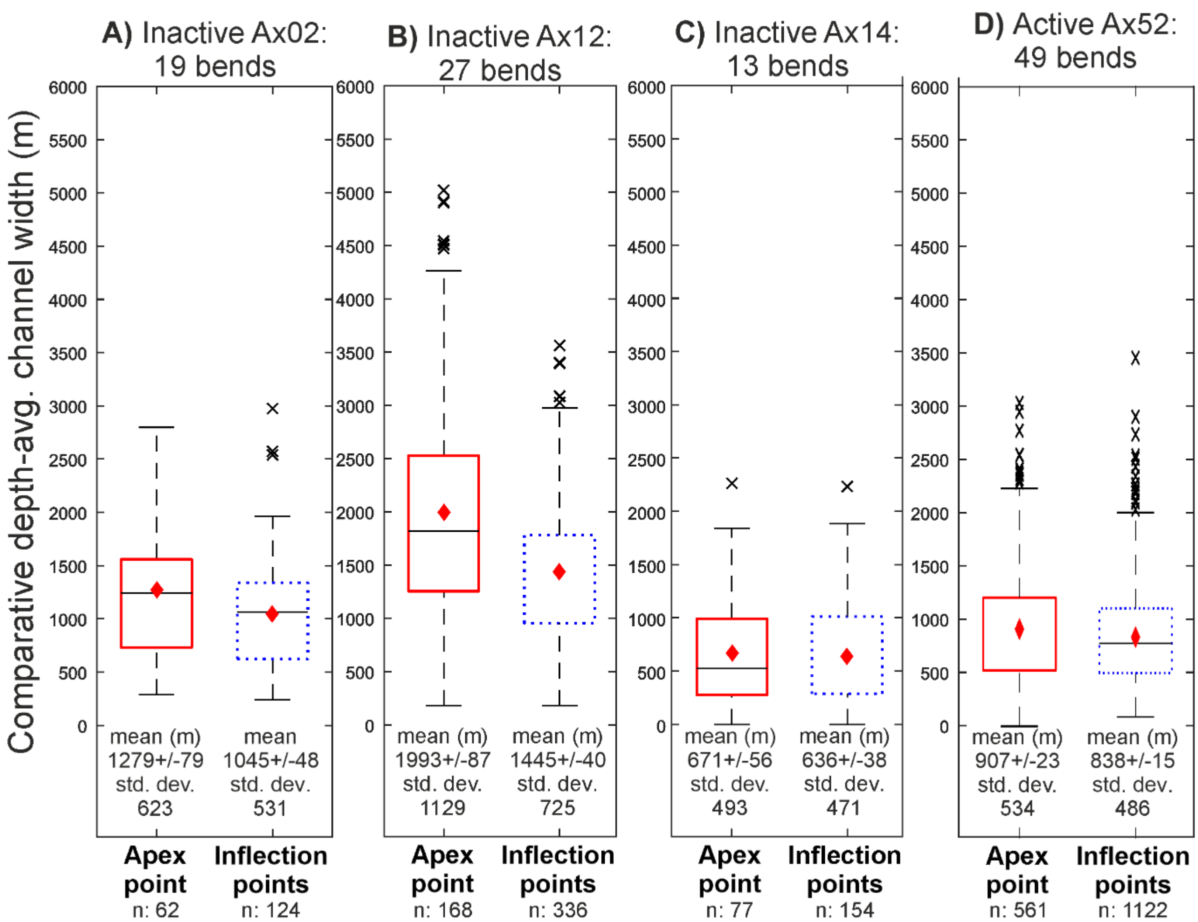

Fig. 9. Box and whisker plots of the comparative depth-avg. channel width between apex point (7a, red solid line) and inflection points (1ui, 13di, blue dotted line) for A) Ax02, B) Ax12, C) Ax14 and D) Ax52. Data include an equal number of measurements per cross-section for each bend and exclude the bank-top channel width. Box indicates 25th and 75th percentiles, “red diamond” indicates the mean, “-” within the box indicates the median, whiskers indicate 99.3% in a normal distribution, and “x” indicate outliers. Mean ± percentage error of the mean, standard deviation (std. dev.) and the number of measurements (n) are shown for each position.

The data on depth-average channel width that incorporates all the points in the vertical are shown in Fig. 10. Bend apices are again shown to be consistently wider than bend inflection positions. Whilst the channel width variations are different in absolute terms to those from the comparative depth-averaged width analysis, the percentage differences are markedly consistent between the two (Ax02, 23% or 315 m wider; Ax12, 38% or 648 m wider; Ax14, 7% or 64 m wider; Ax52, 8% or 90 m; Fig. 10). As with the comparative depth-averaged width data, all of these variations in channel width are statistically significant (p <0.05) except for the narrowest channel Ax14 (Table 3).

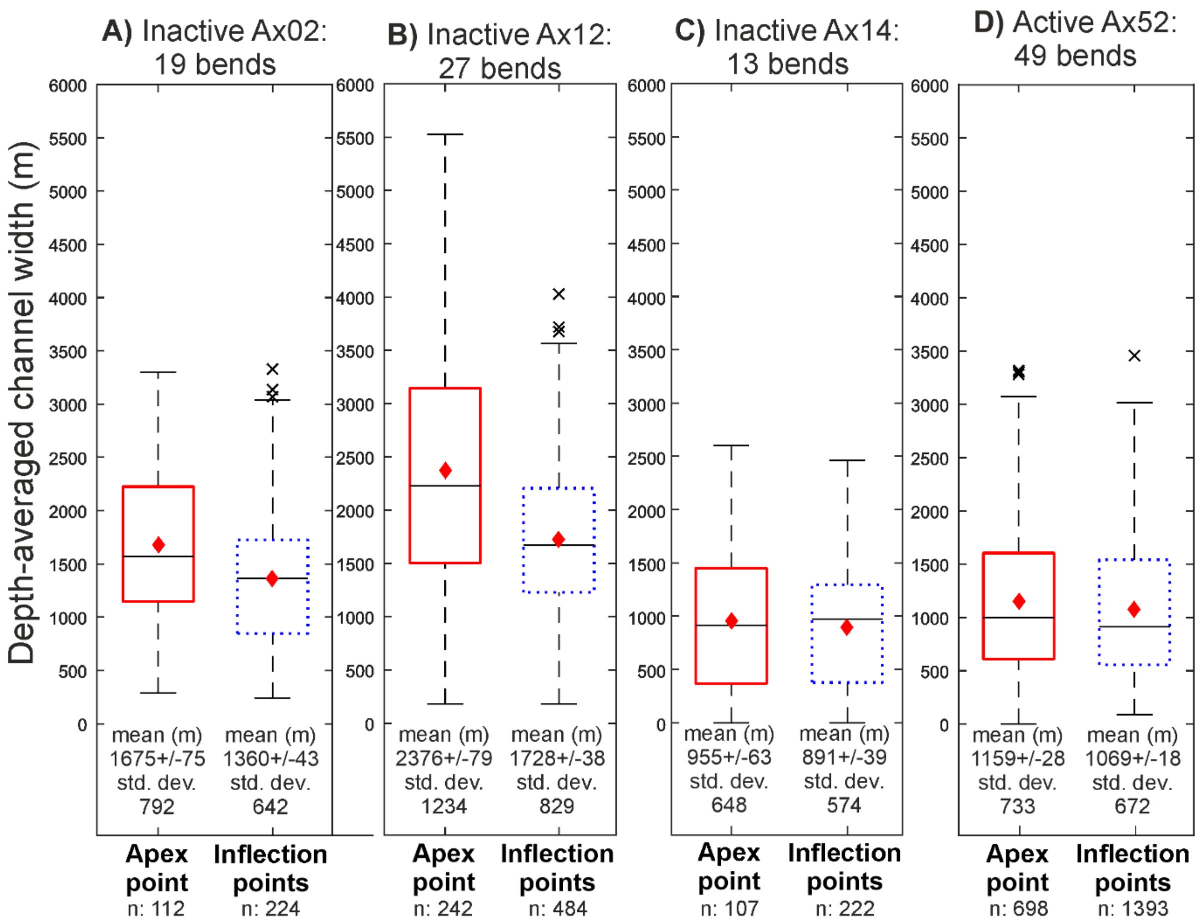

Fig. 10. Box and whisker plots of the depth-averaged channel width between apex point (7a, red solid line) and inflection points (1ui, 13di, blue dotted line) for A) Ax02, B) Ax12, C) Ax14 and D) Ax52. Data include the widths as measured at the height of the inner and outer banks. Box indicates 25th and 75th percentiles, "red diamond" indicates the mean, "-" within the box indicates the median, whiskers indicate 99.3% in a normal distribution and "x" indicate outliers. Mean ±standard error of the mean,

standard deviation (std. dev.) and the number of measurements (n) are shown for each position.

5.1.3 Variation of channel width around bends: bend apex region relative to bend inflection region

Whilst assessing variation in channel width between bend apex and bend inflection points has the advantage of being most comparable to typical river methodologies, this approach may not capture the maximum width, nor provide an assessment of variations around the whole bend. Therefore, here we assess variations between bend apex and bend inflection regions. The bank-top channel width is wider at the apex region than at the inflection region for all submarine channels (Ax02, 9% or 167 m wider; Ax12, 11% or 248 m wider; Ax14, 4% or 64 m wider; Ax52, 1% or 21 m wider; Fig. 11). These variations in channel width between regions are statistically significant ($p < 0.05$) except for the active channel Ax52 (Table 3). This contrasts with bank-top channel width data from the comparison of the apex and inflection points where the bend apex was significantly wider than the bend inflections in the active channel, Ax52.

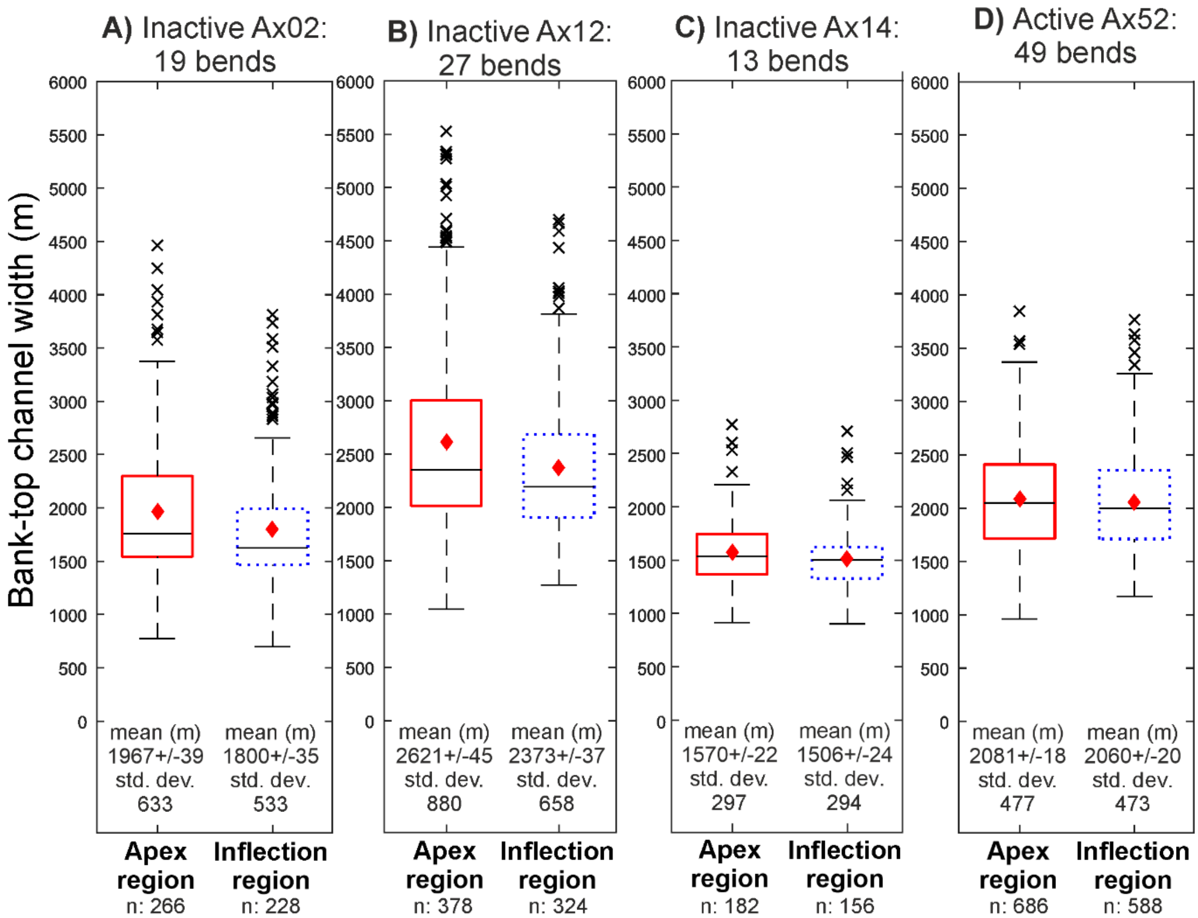

Fig. 11. Box and whisker plots of the bank-top channel width between apex (4u-10d, red solid line) and inflection (1ui-3u, 11d-13di, blue dotted line) regions for A) Ax02, B) Ax12, C) Ax14 and D) Ax52. Data include the widths as measured at the height of the inner and outer banks. Box indicates 25th and 75th percentiles, "red diamond" indicates the mean, "-" within the box indicates the median, whiskers indicate 99.3% in a normal distribution and "x" indicate outliers. Mean ± standard error of the mean, standard deviation (std. dev.) and the number of measurements (n) for each region are shown.

The mean comparative depth-average channel width is also wider at the apex region than at the inflection region for all submarine channels (Ax02, 13% or 139 m wider; Ax12, 11% or 162 m wider; Ax14, 3% or 18 m wider; Ax52, 4% or 32 m wider; Fig. 12).

With the exception of the narrowest channel, Ax14, all of these variations in channel width between regions are statistically significant (p <0.05; Table 3).

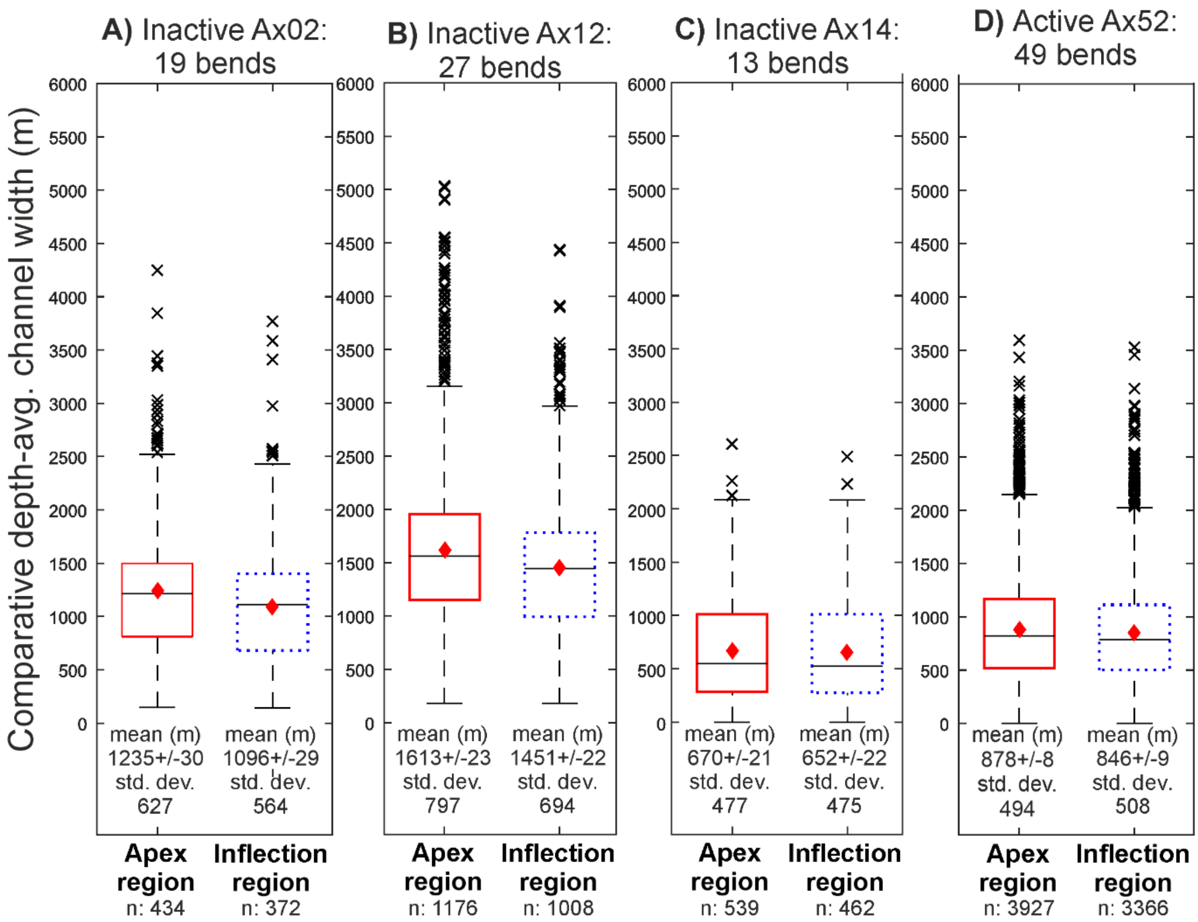

Fig. 12. Box and whisker plots of the comparative depth-avg. channel width between apex (4u-10d, red solid line) and inflection (1ui-3u, 11d-13di, blue dotted line) regions for A) Ax02, B) Ax12, C) Ax14 and D) Ax52. Data include an equal number of measurements per cross-section for each bend and exclude the bank-top channel width. Box indicates 25th and 75th percentiles, “red diamond” indicates the mean, “-” within the box indicates the median, whiskers indicate 99.3% in a normal distribution and “x” indicate outliers. Mean ± percentage error of the mean, standard deviation (std. dev.) and the number of measurements (n) for each region are shown.

Lastly, the mean depth-average channel width is assessed. On this measure, the channel is also wider at the apex region than at the inflection region for all submarine channel reaches (Ax02, 11% or 151 m wider; Ax12, 11% or 189 m wider; Ax14, 1% or 12 m wider; Ax52, 3% or 32 m wider; Fig. 13). With the exception of the narrowest channel, Ax14, all of these variations in channel width between regions are statistically significant (p <0.05; Table 3). As observed with the points data, the two measures of depth-averaged width produce strikingly similar results. In the case of the regions data, not only are the percentage differences similar, but even the absolute magnitude of the variations are very close to one another.

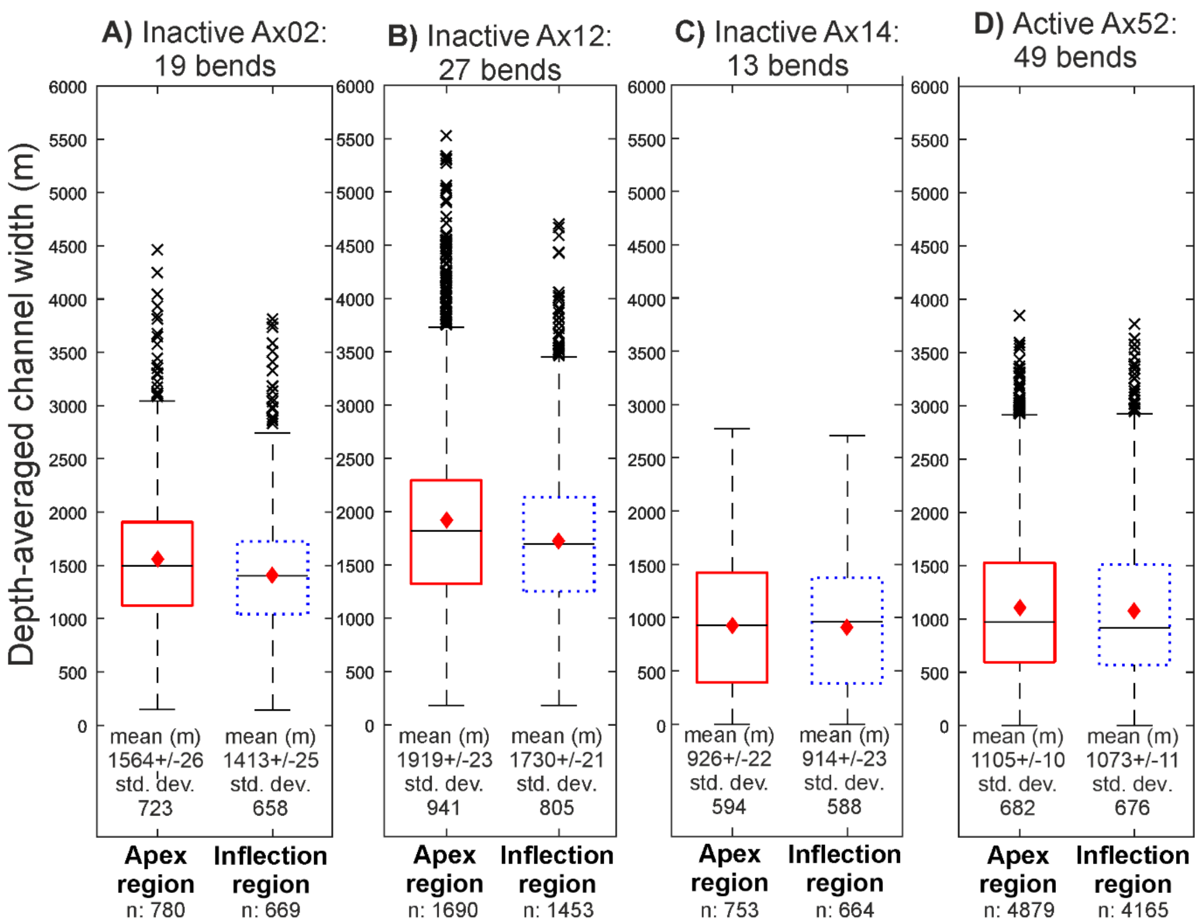

Fig. 13. Box and whisker plots of the depth-averaged channel width between the apex (4u-10d, red solid line) and inflection (1ui-3u, 11d-13di, blue dotted line) regions for A) Ax02, B) Ax12, C) Ax14 and D) Ax52. Data include the widths as measured at the

height of the inner and outer banks. Box indicates 25th and 75th percentiles, “red diamond” indicates the mean, “-” within the box indicates the median, whiskers indicate 99.3% in a normal distribution and “x” indicate outliers. Mean ± standard error of the mean, standard deviation (std. dev.) and the number of measurements (n) for each region are shown.

5.1.4 *Summary of width variations around bends in individual channels*

All three measures of channel width, at both points (bend apex, and bend inflection cross-sections), and regions, produced a consistent result that in all cases the bend apex was wider than the bend inflection (Fig. 14). The magnitude of these variations varied from 1% to 38% depending on the width measure and the channel reach (Fig. 14). For three of the channel reaches, Ax02, Ax12 and the active Ax52, all measures were statistically significant ($p<0.05$), with the one exception of the bank-top channel width for regions, where Ax52 was not significant (Table 3). In contrast, the narrowest channel, Ax14, only showed a significant ($p<0.05$) variation between bend apex and bend inflection width for the two measures of bank-top channel width (points, and regions); the depth-averaged measures were not significant (Table 3). The two-sample t-test therefore rejected the null hypothesis that the apex-width was not larger than the inflection region width, for Ax02, Ax12, Ax52 bar one measure, and for the bank-top channel width measures for Ax14 (Table 3). The alternative hypothesis that the apex width is wider than the inflection width was therefore accepted for almost all cases (Table 3).

Measured variations in channel width between bend apices and bend inflections are two to three times greater when measuring width at bend apex and bend inflections points (6-38% greater at bend apices), than they are for bend regions

(1-13%) (Fig. 14). This indicates that maximum channel width is somewhere close to the bend apex in these systems, and therefore measuring width changes by region has the effect of smoothing out these variations. Nonetheless, even when measured across these regions there remains, in most cases, a statistically significant enhancement in bend apex widths.

The different channel reaches range in the degree to which bends are wider at apices relative to inflections (Fig. 14). The widest channel Ax12 shows the greatest difference between bend apices and bend inflections, with a difference of 36-38% on the apex to inflection points measures, and 11% for regions. Ax02 is the second widest channel on the depth-averaged measures, and also shows a substantial variation between bend apex and inflection, of 22-23% on points measures, and 9-13% for regions. Ax52 is the third widest on depth-averaged measures, although it is wider than Ax02 on bank-top channel width measures. Bend apices are 8-9% wider than inflections for the points data, but only 1-4% wider at regions, of which the 1% difference for bank-top channel width at regions is not statistically significant ($p<0.05$). Finally, Ax14 is the narrowest of the channels, and here only the bank-top channel width variations of 13% (points) and 4% (regions) are statistically significant.

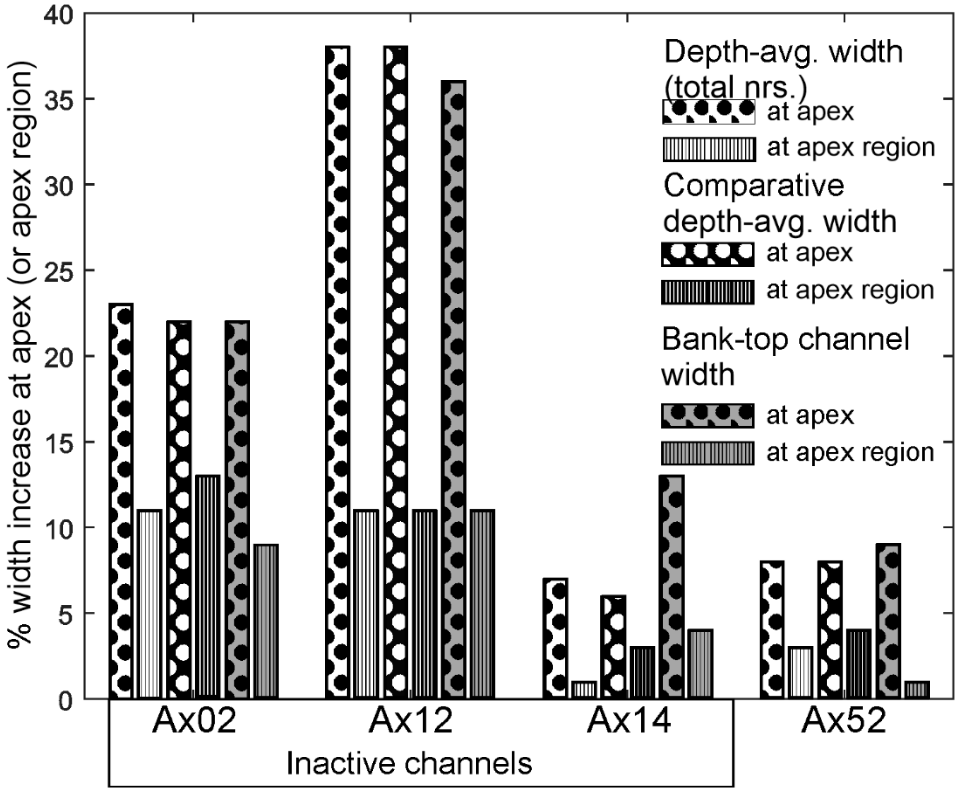

Fig. 14. Bar charts showing the percentage width increase at bend apices compared to the inflection points (symbol: dots), or between apex and inflection regions (symbol: vertical lines), for different measures of channel width. The different width measures are depth-avg. width (symbol: white box), comparative depth-avg. width (symbol: black box) or the bank-top channel width (symbol: grey box). The inactive channels are Ax02, Ax12 and Ax14 and the active channel is Ax52. All results are statistically significant ($p<0.05$) other than both depth-averaged measures for Ax14, and the depth-averaged region data for Ax52 (see Table 3).

Table 3. Results of two-sample Student's t-test between bend apex and bend inflection widths, for a range of different width measurements, for the four channel reaches. The null hypothesis was that the apex-width was not larger than the inflection region width. The table reports p-values, or probability values, that identify whether a statistically significant relationship exist between two sample groups. A p-value of <0.05 identifies a statistical significance between two sample groups with a 95% confidence interval, and rejects the null hypothesis and thus confirms the alternative hypothesis. The alternative hypothesis is that bend apex width is greater than bend inflection width. 'None' represents no significant relationship.

Width measure	**Ax02**	**Ax12**	**Ax14**	**Ax52**
Bank-top channel (points)	<0.005	<0.0005	<0.025	<0.0025
Comp. depth-average (points)	<0.01	<0.0005	None	<0.01
Depth-average (points)	<0.0005	<0.0005	None	<0.005
Bank-top channel (regions)	<0.001	<0.0005	<0.025	None
Comp. depth-average (regions)	<0.001	<0.0005	None	<0.005
Depth-average (regions)	<0.0005	<0.0005	None	<0.025

Lastly, it is noted that the two measures of depth-averaged width, one with an equal number of points for every cross-section (comparative depth-averaged width), and one including all data (depth-averaged channel width) are shown to give very similar results. This indicates that any height variations around channel bends as a result of the enhanced super-elevation in submarine channels, are not unduly biasing the measurement of width variations around bends. Given this result, all subsequent data analysis uses the depth-averaged width data, therefore retaining all of the measured data points. The inclusion of channel banks in the depth-averaged width measurement also enables a reference point for normalisation and comparison of width data from the four channel reaches (see Section 5.2).

5.2. Width variation between channel base and channel banks

The depth-averaged width at both apex and inflection points, and at apex and inflection regions, increases with height above the bed for all submarine channels, but for Ax02 and Ax12 the magnitude of this difference between the width at the apex and at inflections is greater (Figs. 15 and 16). The percentage depth-averaged width variation between the apex and inflections is relatively constant with height for most of the channels, however more variability is shown for Ax14 (Fig. 16).

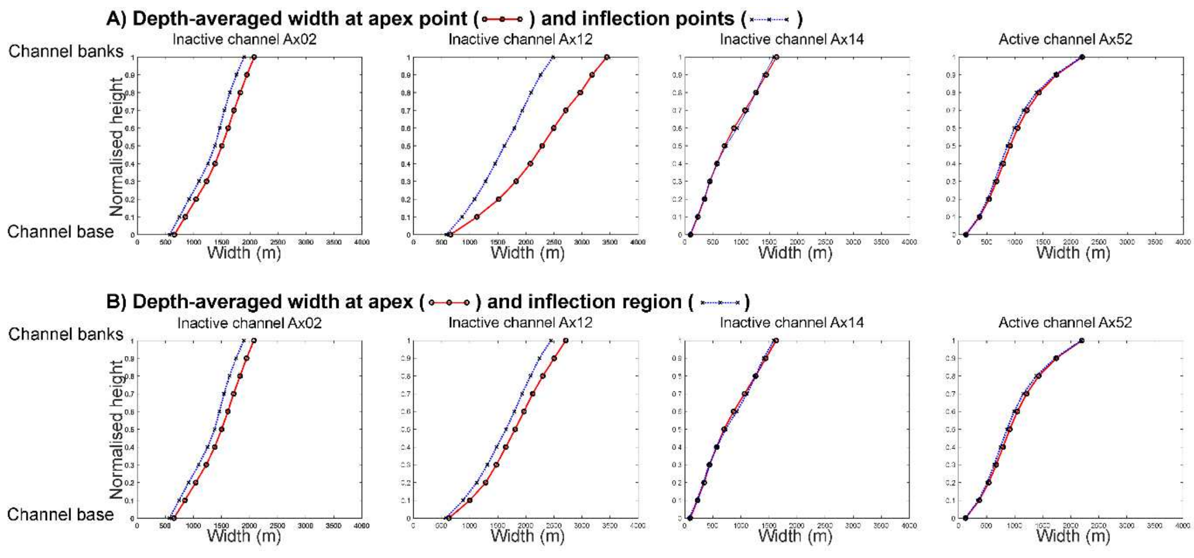

Fig. 15. Depth-averaged width with normalised height at A) apex point (red dashed line) and inflection points (blue dotted line), and B) apex (red dashed line) and inflection region (blue dotted line) for all channel reaches (Ax02, Ax12, Ax14, and Ax52). The normalised height was calculated using the maximum height of each cross-section. Width measurements were calculated by taking the intersection of the normalised height at 0.1 increments with the extracted cross-section profile.

Afterwards the data were averaged. Each data-point corresponds to the average of all bends of a reach.

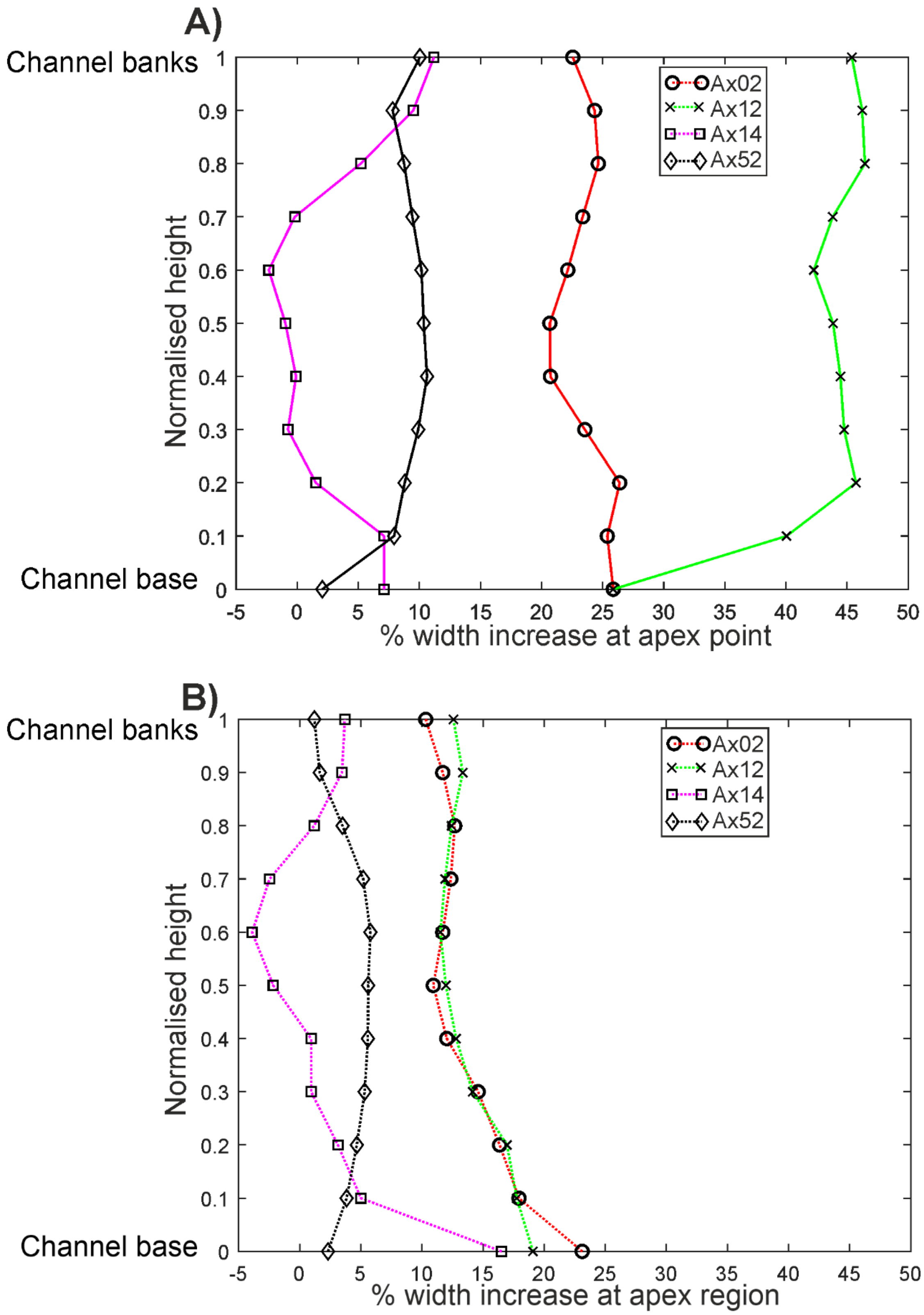

Fig. 16. Percentage width increase at the apex with normalised height, at A) apex point, and B) apex region, for all channel reaches (Ax02, Ax12, Ax14, and Ax52). The normalised height was calculated using the maximum height of each cross-section.

5.3. Channel width variation as a function of sinuosity

Here we assess whether sinuosity and variations in channel width around bends are related. In Fig. 17 the apex-inflection ratio is plotted against sinuosity, with the ratio representing the depth-averaged width at the bend apex region, divided by the depth-averaged width at the bend inflection region, for a given bend. The apex region width was wider than the inflection region width in the majority of cases for bends across all sinuosity classes; straight, low sinuosity, and high sinuosity (Figs. 16 and 17). The majority of bends were classified as straight (n=53), with a more equal distribution between low sinuosity (n=24) and high sinuosity (n=31).

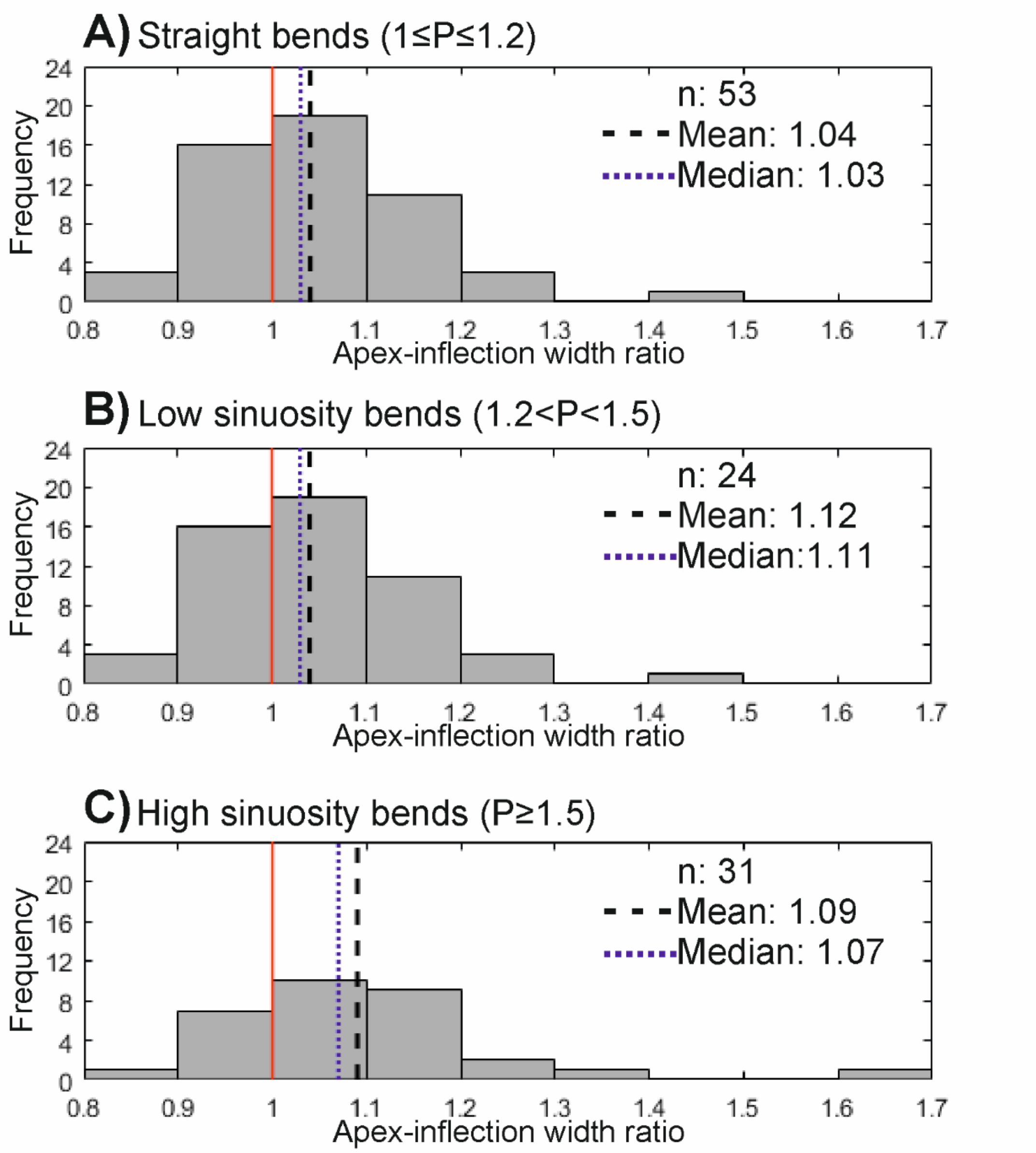

Fig. 17. Bar charts showing the apex-inflection width ratio for A) bends classified as straight (1≤P≤1.2), B) low sinuosity bends (1.2<P<1.5), and C) high sinuosity bends (P≥1.5). Sinuosity was obtained for each bend and corresponds to the ratio between bend length and inflection length (see Fig. 3A).

A second way to assess the relationship between sinuosity and variations in width around channel bends, is to plot mean apex width at regions, against mean inflection width at regions, as a function of sinuosity classes (Fig. 18). The linear regression varied little between bends classified as straight, low sinuosity, and high sinuosity, suggesting that there is little if any relationship between sinuosity and a wider apex region width (Fig. 18). No difference is seen between different channel reaches.

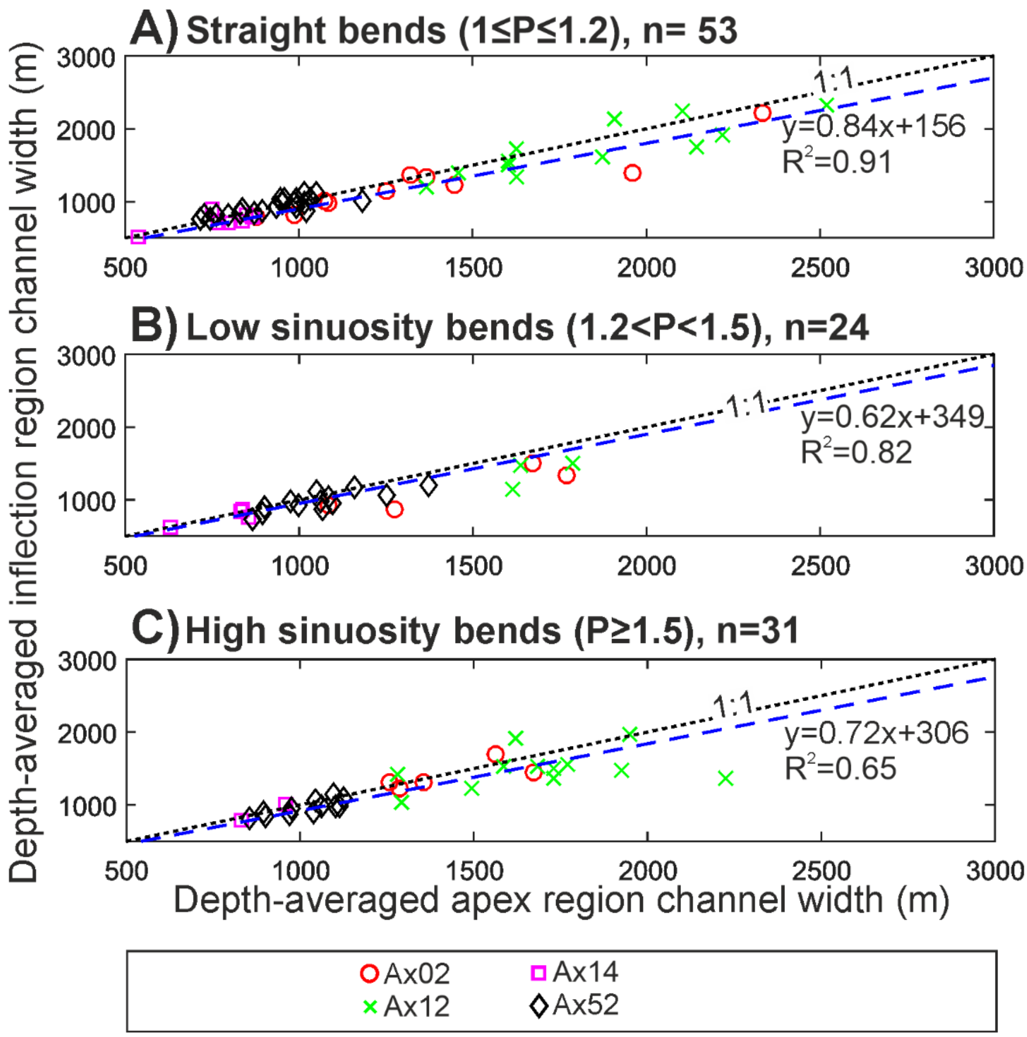

Fig. 18. Depth-averaged apex region width versus depth-averaged inflection region width for A) bends classified as straight (1≤P≤1.2), B) low sinuosity bends (1.2<P<1.5), and C) high sinuosity bends (P≥1.5). The following channels were used: Ax02 (19 bends, circle), Ax12 (27 bends, cross), Ax14 (13 bends, square) and Ax52 (49 bends, diamond). Each point represents one bend and contains measurements from the

depth-averaged channel width. Sinuosity was obtained for each bend and corresponds to the ratio between bend length and inflection length (see Fig. 3A).

5.4. Channel width variation as a function of radius of curvature

The relationship between the percentage bank-top channel width increase at the bend apex point relative to inflection points is plotted as a function of radius of curvature normalised by the bank-top channel width (Fig. 19). These data can be fitted by an envelope that describes the maximum width increase at bend apices relative to inflections for a given normalised radius of curvature. This envelope shows that channel apices are at their widest relative to inflections for tight bends, peaking at a radius of curvature-channel width ratio between 0.3 and 0.4 for Ax02, Ax12 and Ax52 and slightly above 0.4 for Ax14.

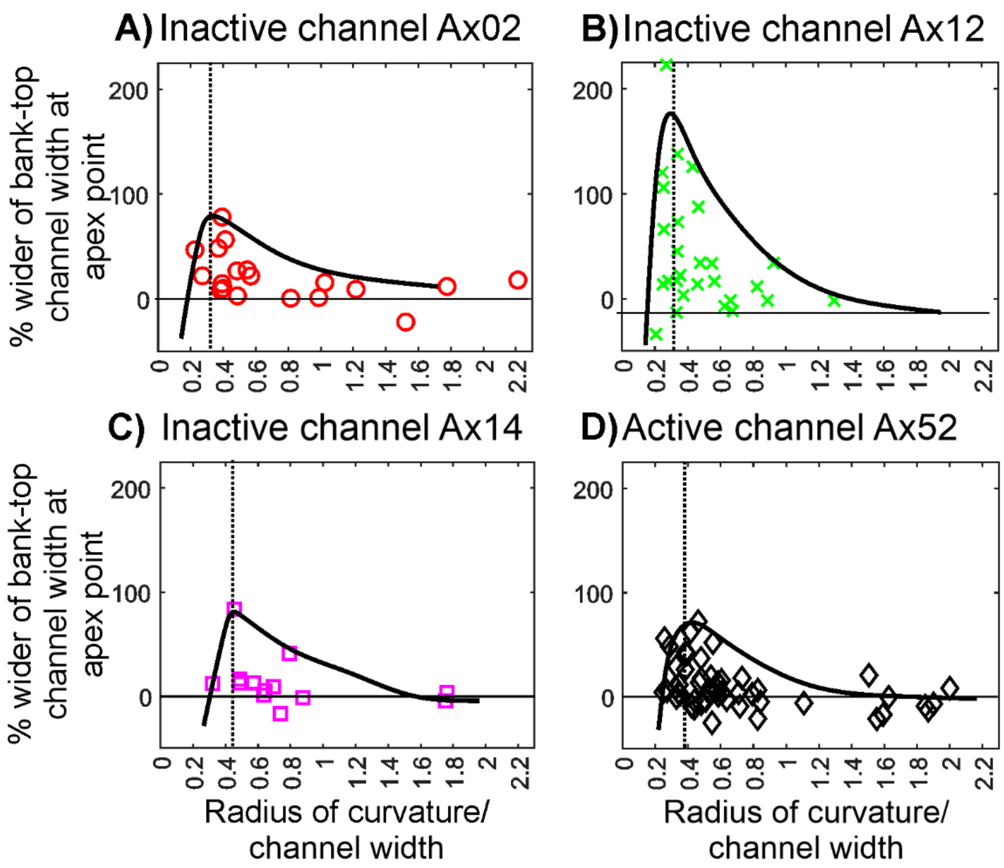

Fig. 19. Relationship between the percentage bank-top channel width increase at the bend apex point relative to inflection points, and the ratio of radius of curvature to bank-top channel width, is shown for A) Ax02 (19 bends), B) Inactive channel reach Ax12 (27 bends), C) Inactive channel reach Ax14 (13 bends) and D) Active channel

reach Ax52 (49 bends). Each point represents one bend. The radius of curvature was measured for each bend using the curve-fitting method (Brice, 1973, 1974) along the channel base centreline. The channel width is the bank-top channel width of the 13 cross-sections along the bend.

5.5. Overall trend of channel width variation around bends

A strong correlation is observed between the mean depth-averaged apex region width and the mean depth-averaged inflection region width (Fig. 20A) with an R^2 value of 0.85 (linear) for all 108 bends from the four channel reaches. The majority (70%) of bends (76 from 108 bends) were on average 161 m or 10% wider at the apex region compared to the inflection region. For the remaining 32 bends, the inflection region was on average 92 m or 7% wider compared to the apex region. Bends with terraces or no terrace present at the inner bend had a similar trend (Fig. 20B) with an R^2 of 0.83 (terrace) and 0.81 (no terrace). Bends without terraces exhibited slightly wider bends at apex regions relative to bend inflection regions, compared with those bends with terraces, for bends greater than 1000 m wide.

80% of bends from the inactive channel reaches are wider at the apex region (Fig. 21; 17 out of 19 bends for Ax02, 21 out of 27 bends for Ax12 and 9 out of 13 bends for Ax14) with R^2 values between 0.50 and 0.78, whereas the active channel reach has 59% of bends wider at the apex region (Fig. 21; 29 out of 49 bends for Ax52), with an R^2 value of 0.7.

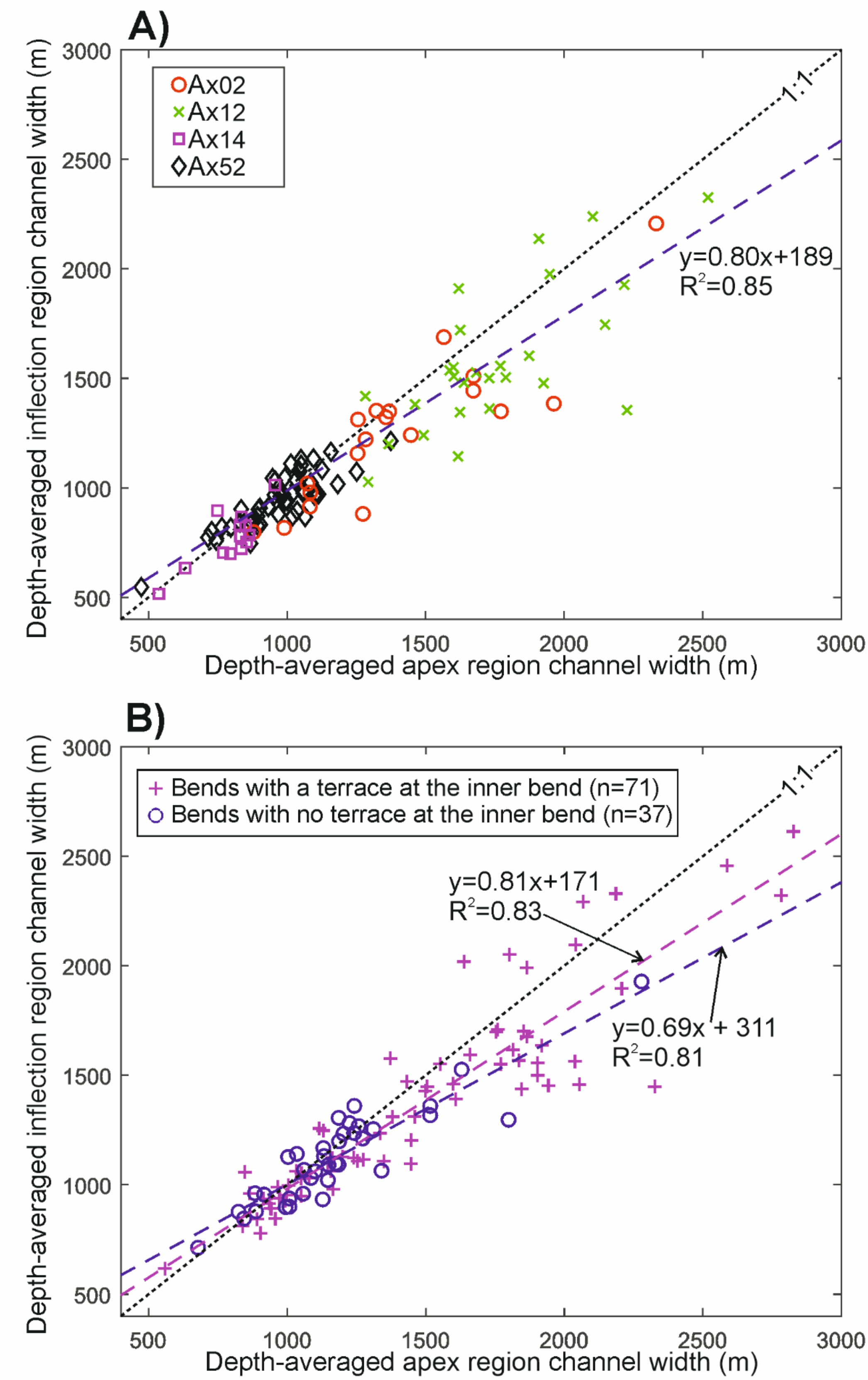

Fig. 20. A) Mean apex-region width versus mean inflection region width. Each point represents one bend and contains measurements of the depth-averaged channel

width. The mean width for a bend was obtained from six cross sections for mean inflection-region and seven cross-sections for mean apex region width. A high correlation (blue dashed line, R^2=0.85) is shown. The active channel reach is Ax52 (49 bends, diamond). Inactive channel reaches are Ax02 (19 bends, circle), Ax12 (27 bends, cross) and Ax14 (50 m resolution, 13 bends, square). B) Mean apex region width versus mean inflection region width for bends with terraces present or not. Bends with a terrace (cross) had an R^2 of 0.83 and bends with no terrace (circle) had an R^2 of 0.81. Black dotted line represents an equal mean inflection region and apex region width.

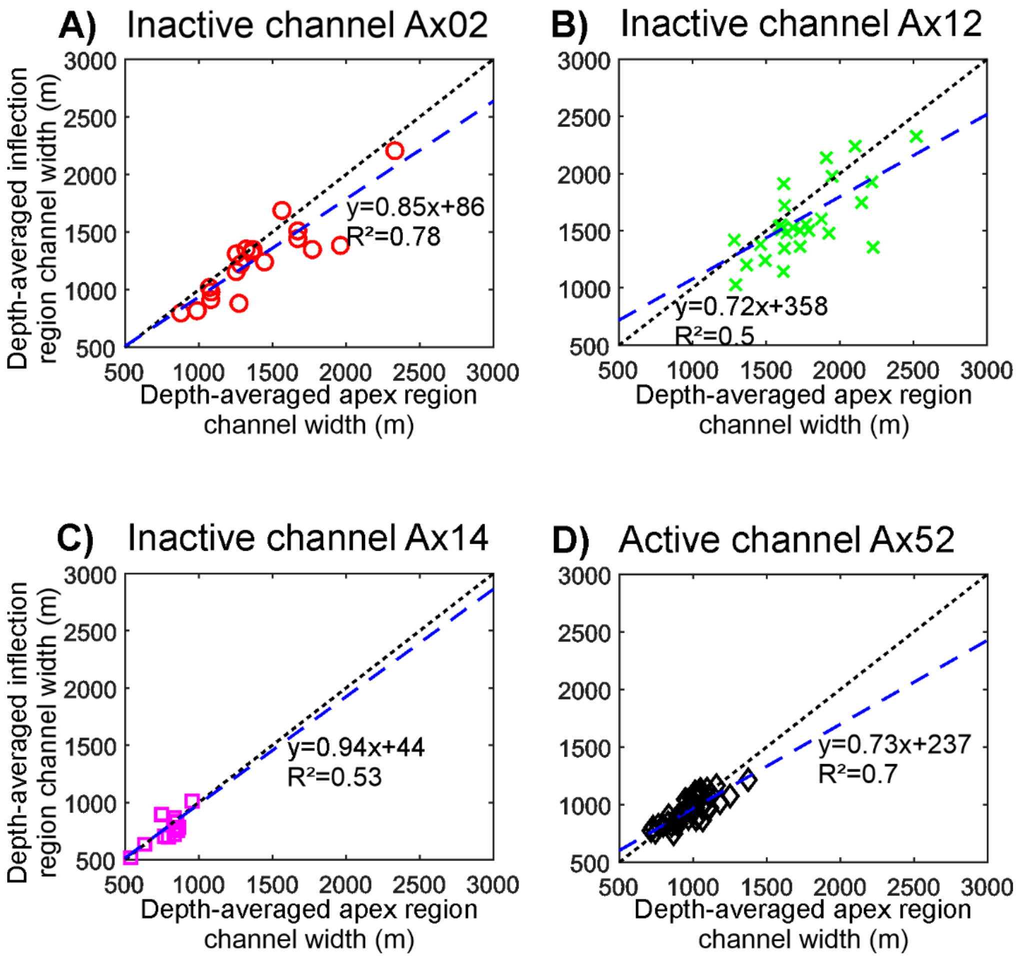

Fig. 21. Mean apex region width versus mean inflection region width. Each point represents one bend and is based on depth-averaged measurements. Blue dashed line represents the linear regression and black dotted line represents equal mean apex and inflection region width. A) Active channel reach Ax52 (49 bends), B) Inactive channel reach Ax02 (19 bends), C) Inactive channel reach Ax12 (27 bends), and D) Inactive channel reach Ax14 (13 bends).

---

6. Discussion

We have presented clear evidence in inactive and active reaches of the Congo channel that submarine channel bends are significantly wider at bend apices than they are at bend inflections, for both points and regions. Here we explore how these results compare to alluvial river channels, and examine the implications for sedimentation at channel bends, and bend evolution. The question of whether these channels are dominated by bank pull or bar push processes is then examined. Lastly, we assess the potential role of climate forcing in controlling variations in width around bends.

6.1. Comparison of submarine channel bends to river bends

In order to directly compare these submarine channels to the results obtained from sinuous point-bar rivers (type C of the Brice (1975) classification; Lagasse et al., 2004; Eke et al., 2014a), the mean width at the channel banks, which is equivalent to bankfull level in rivers (Clark et al., 1992; Pirmez and Imran, 2003; Konsoer et al., 2013), from the inflection points and apex point is taken. The results show that bend apices for the Congo channel reaches had bank-top channel widths that were between 9 and 36% greater than bend inflections. This compares to a 14% increase in width at the apex point for rivers as observed by Eke et al. (2014a). However, this width difference may be an overestimation for submarine channels as they exhibit lower gradient banks than rivers (rather V-shaped cross-sections; Islam et al., 2008). If we assume that the rivers essentially have vertical banks, then a more appropriate comparison for submarine channels may be the depth-averaged widths at the bend apex and inflection points. However, the Congo channels exhibit a very similar variation as for the bank-top channel widths, with bend apices 7-38% wider than bend inflections.

There may be ambiguity by looking solely at the apex and the two inflection points for both rivers and submarine channels as comparison between regions might be a better guide to the width variations around bends as this approach acts to smooth out outliers at the apices and inflections. However, it is not possible to directly compare such figures to the data from rivers. A simpler measure is to compare the number of bends that are wider at the apex point/region, and in this respect the observed submarine channels from Axial Congo Fan are similar to rivers (60% wider at apex point; Eke et al., 2014a), with active channel reaches very similar (59% wider at apex point/region) and inactive channel reaches a little higher (70%-89% wider at apex point, 62%-84% wider at apex region) based on depth-averaged widths.

The results from the apex and inflection points suggest that there is an increased variation in width changes around bends for Ax02 and Ax12 (23% and 38% greater at bend apices in terms of depth-averaged width; 22-36% for bank-top channel width), whereas Ax14 and Ax52 exhibit a smaller variation (7-8%, and 9-13% on the same measures) respectively, compared to sinuous point-bar rivers (Eke et al., 2014a, b). The reason(s) for a difference in width variation between rivers and Ax02 and Ax12 and also within/between submarine channels is unclear. Possible explanations include super-elevation which is around two orders of magnitude greater compared to rivers (Dorrell et al., 2013), and may vary between submarine channels and within submarine channels. Strong overspill related to super-elevation can lead to sandier deposits at the outer bank, forming spillover lobes and sediment waves (Nakajima et al., 1998; Wynn and Stow, 2002; Posamentier, 2003; Morris et al., 2014a). Sediment waves resulting from this overspill have been observed in the Congo system (Migeon et al., 2004). Potentially these less cohesive sandier deposits may be more erodible than equivalent outer bank deposits in rivers. Asymmetry in exhumed levees has been reported (Kane and Hodgson, 2011), with outer bank external levees being thicker and having a higher sand content. Furthermore, erodibility of submarine levees would be enhanced in systems prone to avulsion and progradation, such as the Congo, where the base of the levee is commonly a sand-prone frontal lobe (e.g. Morris et al., 2014b;

Picot et al., 2016). Alternatively, such variation between bank erodibility might be related to strongly variable flow structures and induced shear stresses. The 3D-helical flow structure in submarine channels is composed of a downstream primary flow component, and a cross-stream secondary flow component, as in rivers (e.g., Peakall and Sumner, 2015; Davarpanah Jazi et al., 2020; Wells and Dorrell, 2021). However, the orientation of the helix is frequently reversed relative to rivers, with basal flow at bend apices going from the inner to outer bank (e.g., Peakall and Sumner, 2015; Dorrell et al., 2018; Wells and Dorrell, 2021). Experiments and simulations have shown that this reversal in secondary flow causes the downstream flow velocity core (the area with the highest downstream velocities) to increase in magnitude and be moved towards the outer bank (Keevil et al., 2006; Giorgio Serchi et al., 2011). This movement of the downstream flow core may intensify outer bank erosion. However, it remains unclear how the position and strength of the downstream velocity core varies between rivers and submarine channels, and between submarine channels. Reversal of the secondary flow field does lead to flow impinging (impacting at an oblique angle) on the outer bank further around the bend than in rivers, at least for constant width channels (e.g. Keevil et al., 2006), and again this may cause enhanced erosion at the outer bank due to deflection of the flow towards the outer bank.

One might expect these factors to apply to all of the submarine channels, yet there is a lot of variation between the channel reaches. We return to this question at the end of the discussion where we consider possible differences in external forcing between channels.

6.2. Sedimentation at channel bends

The evidence for wider bend apices has profound implications for sedimentation within submarine channels. Point-bars are often not observed in submarine channels, likely because such tractional forms only form when migration is rapid relative to aggradation (Sylvester et al., 2011). However, where present, observations from fixed width channel experiments (Peakall et al., 2007; Amos et al., 2010; Wells and Cossu, 2013; Cossu and Wells, 2013) and simulations (Darby and Peakall, 2012), suggest that point-bars are preferentially formed downstream of bend apices. This position beyond the bend apex is because, as noted earlier, secondary circulation is frequently reversed in turbidity currents relative to river channel flows (Corney et al., 2006, 2008; Dorrell et al., 2013; Peakall and Sumner, 2015), and this leads to flow being outwardly directed for further around the bend than in rivers. These experiments and simulations also exhibit tight bends where there may be an enhanced phase lag between curvature and secondary flow strength (Zhou et al., 1993; Ezz and Imran, 2014). As a consequence, the point at which flow and sediment flux converge, in turn driving sedimentation and point-bar development (Nelson and Smith, 1989), is beyond the bend apex, rather than dominantly at the bend apex as in rivers (Peakall et al., 2007; Amos et al., 2010; Peakall and Sumner, 2015).

This delay in the convergence of flux at the inner bend as a result of reversed secondary circulation will still occur in natural submarine channels but the increased width at the bend apex will affect the flow dynamics. The increased width at bend apices will lead to a reduction of the outwardly directed centrifugal force in the upstream part of the bend where channel width is increasing, leading to reduced flow super-elevation relative to constant width channels, and a corresponding decrease in the pressure gradient force at the base of the flow. Past the bend apex as the channel narrows, super-elevation and the pressure gradient force will be maintained for longer than in a constant width channel, and the flow towards the inner bank will be enhanced; in turn these aspects will lead to flow convergence and traction-dominated sedimentation further upstream than in fixed width channels (cf. Nelson and Smith, 1989). Interestingly, channel width at bend apices relative to inflections increases to a maximum for bends where radius of curvature is relatively small (Fig. 19), suggesting that as bends tighten the channel undergoes adjustment therefore reducing the associated increase in centrifugal forces, and enhancing the flow patterns described above. For suspension-driven deposition, increasing width at bend apices, particularly at tight bends where apices are relatively widest, is likely to further enhance flow separation at the inner bank relative to that observed in fixed width channels (Straub et al., 2008, 2011b; Janocko et al., 2013; Basani et al., 2014), thus driving sedimentation and formation of oblique accretion deposits at the inner bend (Straub et al., 2011b; Peakall and Sumner, 2015). Such suspension-dominated sedimentation is in keeping with observations of modern and ancient submarine channel-fills where low-angle, inclined, low-amplitude (fine-grained in ancient examples), sediments are observed at inner bends, often above thinner point-bar deposits (Schwenk et al., 2005; Deptuck et al., 2007; Babonneau et al., 2010; Hodgson et al., 2011; Kolla et al., 2012; Peakall and Sumner, 2015).

Taken together, the effects of wider channel apices on tractional- and suspension-driven sedimentation will result in point-bar development much closer to the bend-apex (Fig. 22). This result suggests resolution of a contradiction at the heart of our understanding of submarine channel bend development. Theoretical, experimental and numerical work have all indicated that point-bar development is further downstream in submarine channels than in rivers, which would be expected to be associated with bank erosion beyond the bend apex and enhanced downstream migration (sweep; Peakall and Sumner, 2015). However, planform studies of aggradational channels on passive margins have paradoxically long indicated that bend development is instead dominated by bend amplitude growth (swing; Peakall et al., 2000a, b; Jobe et al., 2016). Our understanding has been based on an absence of knowledge of width variation in submarine channels, and thus has assumed the simplest possible case, that of fixed width channels (i.e. canaliform). As shown here for the Congo submarine channels, a width variation does occur, with bend apices typically wider than inflections, and this clearly has important ramifications, leading to deposition closer to bend apices (Fig. 22). Consideration of width variation changes around submarine bends and their likely influence on sedimentation appears to be the 'missing link' for a holistic understanding of bend dynamics in submarine channels.

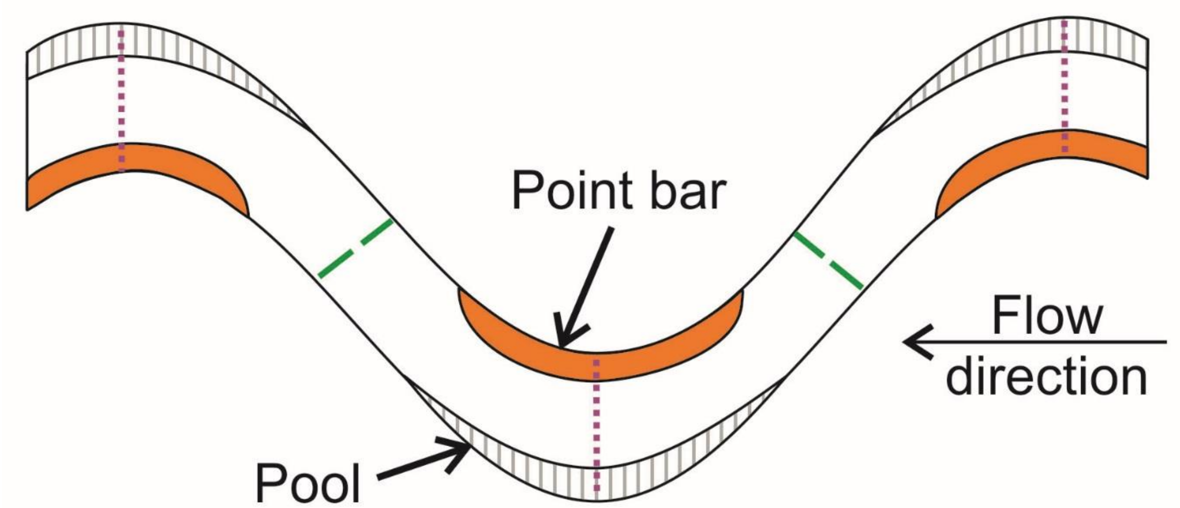

Fig. 22. Summary diagram of submarine channels illustrating that they are wider at bend apices compared to inflections. Purple dotted line represents apex cross-section and green dashed lines represent inflection cross-sections. Postulated positions of maximum erosion (white area) and aggradation (black area) are shown. This schematic diagram also suggests that point bars and zones of outer bank erosion are

located more symmetrically around the bend apex, rather than prominently downstream of the bend apex; for channels without significant external tectonic or topographic influence.

6.3. Bank pull or bar push?

The clear and consistently wider bend apices relative to inflections, observed in these Congo channels, are consistent with actively migrating channels, as observed in rivers. However, there is a question as to what is driving this migration. Is this a result on inner bend deposition (bar push) or outer bank erosion (bank pull)? Point-bar deposits composed of high amplitude deposits are relatively thin in the Congo channels, in the small number of examples where data allows them to be recognised (Babonneau et al., 2010). This is in keeping with other submarine channels, where point-bars, if present, typically do not scale with flow depth as they do in alluvial rivers (Nakajima et al., 2009; Darby and Peakall, 2012). Overlying these high amplitude deposits are vertically accreting, low-angle inclined finer-grained units that have similar seismic response to the external levee deposits (Babonneau et al., 2010). The geometry of these finer-grained deposits suggests that they were deposited after the initial formation of the point-bar (Babonneau et al., 2010). Consequently, only deposition of the thin point-bar deposit could act as bar push, and it is not clear if this would be sufficient to control channel migration. The overlying finer-grained material is filling in space at the inner bank, and thus is responding to bank pull at that level. The presence of very wide bend apices relative to inflections as observed in Ax02 and Ax12 casts further doubts on the applicability of bar push in this system. Instead such width variation, suggests that bank pull may be the dominant process here, leading to the creation of space at the inner bend. Given the thin point-bars, this may also be the case for Ax14 and Ax52 with their smaller relative increases in width at bend apices compared to inflections. These observations, notably the marked increases in channel width at bend apices, support the conceptual ideas of Peakall and Sumner (2015) who previously suggested that submarine channels may be controlled by bank pull as submarine channels frequently do not have point bars and in many cases the inner bend deposits are instead composed of finer-grained deposits analogous to oblique accretion deposits in mixed load rivers. We therefore suggest that submarine channels may be dominated by bank pull, in contrast to rivers where there is evidence for both bar push and bank pull depending on the system (e.g., Constantine et al., 2014; Eke et al., 2014a,b; Van de Lageweg et al., 2014; Donovan et al., 2021).

6.4. Control on width of submarine channel bends

The results of this study, in combination with the theoretical arguments of Peakall and Sumner (2015), suggest that bank pull, and channels that have wider bend apices, are likely typical for submarine-fan channels. One key question is whether the variation in channel width, caused by the ratio of the relative rates of erosion at the outer bank, and deposition at the inner bank (Eke et al., 2014a, b), is a function of flow properties such as sediment yield and composition, and volume, and by extension the type of turbiditic flows. If such flow properties are a key driver, then changes in channel width would be expected geographically, and for a given system then changes over time are predicted if affected by allogenic forcing. The present dataset allows this question to be examined. Monsoonal cycles have been linked to the architectural cycle of the Congo Fan for the last 40 kyr (Picot et al., 2019). Picot et al. (2019) suggest based on pollen assemblages (proxy for vegetation cover), kaolinite/smectite (K/S) ratio (proxy for freshwater plume intensity and thus discharge of the Congo River), and monsoon index, that prograding periods are related to an increase in monsoonal intensity and therefore humidity and freshwater input. Furthermore, retrograding periods are related to a low monsoonal intensity and hence decrease in humidity and freshwater input. Picot et al. (2019) identified three types of monsoonal periods in the last 40 kyr: arid, humid, and transition monsoonal period from humid to arid. During arid monsoonal periods there is low discharge, increased sediment yield (Jansen et al., 1984), and more coarse sediment relative to mud, which leads to a low transport capacity of turbidity currents and channel infill. In contrast, humid periods correspond to higher discharge, and reduced sediment yield (Jansen et al., 1984) producing clays and a higher mud/sand ratio, which leads to high capacity turbidity currents and probably increased confinement by channel erosion and levee construction (Picot et al., 2019). A transitional monsoonal period from arid to humid causes the retrogradation due to an increase in precipitation and river runoff, prior to re-establishment of vegetation, which increases erosion and coarse sediment production, and hence channel infill.

Here, we utilise the degree to which the apex is wider than the inflections based on depth-averaged width measurements for each channel. A relative age constraint for each channel (Picot et al., 2019) is then utilised and compared to a monsoonal cycle extending over the past 200 kyr, as predicted by numerical models (Caley et al., 2011), which gives an environmental setting during channel formation (Fig. 23). The assumption is made that the relationship between monsoon period and progradation/retrogradation identified by Picot et al. (2019) for the past 40 kyr, holds over this 200 kyr period and that the width measurements are interrelated to the monsoonal cycle. It must be noted that this comparison has a number of assumptions including a small sample size. However, it might explain width variations between different submarine channels. Ax14 was formed during a retrograding period at the beginning of cycle B during a peak dry monsoonal period (Picot et al., 2019). An arid climate may have led to flow sizes and capacity being small, and therefore less sediment being eroded at outer banks, which would have led to a narrow apex (7% wider depth-averaged width at the apex point relative to the inflection points). Ax12 may have occurred during an arid to humid period with a peak prograding phase at the end of cycle A (Picot et al., 2019), and so flow sizes and capacity would have increased, and more sediment was likely subsequently eroded at outer banks. Hence, the apex was comparatively wide (38% wider depth-averaged width at the apex point relative to the inflection points). Ax02 also has a high apex width (23% wider on the same measure) as it occurred at the beginning of the prograding period of cycle A which follows a retrograding peak. An increase in river freshwater input and a decrease in solid discharge at the beginning of the progradation that follows the retrogradation maximum may explain the increase in capacity of turbidity currents and a high apex-region width for Ax02. Lastly, the active channel Ax52 occurred during the maximum progradation of cycle D, which correlated with a transition towards a more arid west African monsoonal system (Fig. 23; Caley et al., 2011), where vegetation cover and river liquid and solid discharge decrease and hence sediment capacity reduced, which would fit with the apex-region width being comparatively low (8% wider on the same measure). All of these comparisons assume that there is no significant change in submarine channel cross-sectional morphology during the process of avulsion and shutdown. For instance, smaller flows may be expected to run up and deposit their sediment on outer banks, potentially forming outer bank bars (Nakajima et al., 2009). That said, the variations between different climatic conditions is probably greater than channels being currently active or not, and hence the data may suggest that there is a relationship between channel bend variation and turbiditic flow characteristics driven by climatic conditions. In summary, turbidity currents with enhanced transport capacity appear to be associated with channels with an enhanced width variation, with wider bend apices relative to inflections.

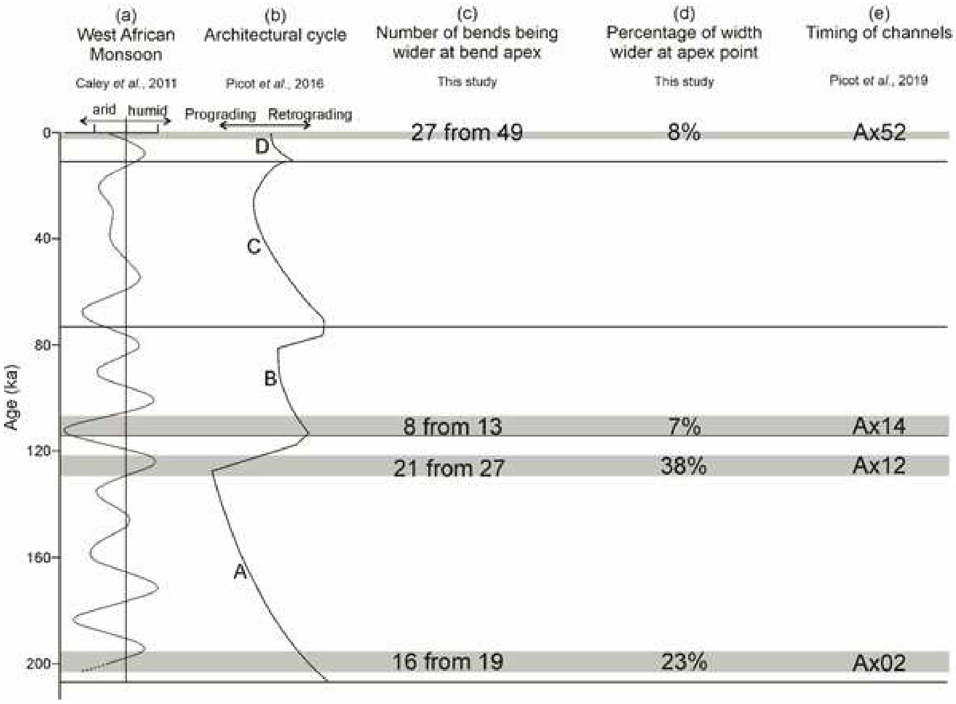

Fig. 23. Relationship between climate, progradation/retrogradation, and channel bend width variations. Aspects modified from Caley et al. (2011) and Picot et al. (2016, 2019). Channel bend width variations are based on depth-averaged width measurements from the apex point and inflection points.

7. Conclusions

This study has analysed the nature of cross-sectional width variation around submarine channel bends, from both active and inactive channels on the Congo Fan. All the studied submarine-fan channels were dominated by bends where the apex is wider than the inflections, which is similar to actively migrating meandering rivers. The result that bends are in general wider at bend apices, combined with consideration of depositional processes, suggests that bend migration in submarine channels is controlled by outer-bank erosion (bank pull) rather than by inner-bend deposition (bar push). A key paradox in our understanding of the dynamics of aggradational submarine channels has been that field observations typically indicate dominantly lateral bend expansion, whilst laboratory and numerical models predict downstream translation of bends. In the absence of any data, and for simplicity, all numerical and experimental work has assumed constant width channels. Herein it is shown that this assumption is incorrect, and increased channel width at bend apices provides an answer to this paradox. The three-dimensional flow dynamics in bends with wider bend apices are predicted to lead to the locus of tractional sedimentation, in the form of point-bars, moving towards the bend apex, compared to that modelled in previous process studies. Enhanced flow separation in bends also likely leads to suspension-driven sedimentation in the additional space at the inner bend. Asymmetry in the erodibility of the outer and inner banks due to super-elevation and overspill of sandier parts of flows will further enhance bank pull dynamics. Comparison of the morphological changes between channels and the climate conditions at the time of their formation, suggests that there may be a relationship between channel bend variation and climatic-driven variation in sediment source composition and turbiditic flow characteristics. Flows with a higher transport capacity appear to be associated with channels with an enhanced width variation, with wider bend apices relative to inflections.

Declaration of Competing Interest

The authors confirm that they have no competing interests.

Acknowledgements

This work was financially supported by the Leeds Anniversary Research Scholarships. We would like to thank B. Loubrieu (IFREMER) for the extraction of the DTM used in this study, and David Lee for help with several of the figures. We thank the four anonymous reviewers for their constructive reviews and the editor Michele Rebesco. Additionally, we would like to thank Nigel Mountney and Christopher Stevenson for suggestions on a previous version of this paper.

References

Amos, K.J., Peakall, J., Bradbury, P.W., Roberts, M., Keevil, G., Gupta, S., 2010. The influence of bend amplitude and planform morphology on flow and sedimentation in submarine channels. Mar. Pet. Geol. 27, 1431–1447. https://doi.org/10.1016/j.marpetgeo.2010.05.004

Azpiroz-Zabala, M., Cartigny, M.J.B., Talling, P.J., Parsons, D.R., Sumner, E.J., Clare, M.A., Simmons, S.M., Cooper, C., Pope, E.L., 2017. Newly recognized turbidity current structure can explain prolonged flushing of submarine canyons. Sci. Adv. 3, e170020. https://doi.org/10.1126/sciadv.1700200

Babonneau, N., Savoye, B., Klein, B., 2002. Morphology and architecture of the present canyon and channel system of the Zaire deep-sea fan. Mar. Pet. Geol. 19, 445–467. https://doi.org/10.1016/S0264-8172(02)00009-0

Babonneau, N., Savoye, B., Cremer, M., Bez, M., 2004. Multiple terraces within the deep incised Zaire Valley (ZaiAngo Project): are they confined levees?, in: Lomas, S.A., Joseph, P. (Eds.), Confined Turbidite Systems. Geol. Soc. London Spec. Publ., 222, pp. 91–114. https://doi.org/10.1144/GSL.SP.2004.222.01.06

Babonneau, N., Savoye, B., Cremer, M., Bez, M., 2010. Sedimentary architecture in meanders channel: detailed study of the present Congo Turbidite Channel (ZaiAngo Project). J. Sediment. Res. 80, 852–866. https://doi.org/10.2110/jsr.2010.078

Basani, R., Janocko, M.J., Cartigny, M.J.B., Hansen, E.W.M. Eggenhuisen, J.T., 2014. MassFLOW-3D$^{\mathrm{TM}}$ as a simulation tool for turbidity currents, in: Martinius, A.W., Ravnås, R., Howell, J.A., Steel, R.J., Wonham, J.P. (Eds.), Depositional Systems to Sedimentary Successions on the Norwegian Continental Margin. International Association of Sedimentologists Special Publication, 46, pp. 587–608. https://doi.org/10.1002/9781118920435.ch20

Braudrick, C.A., Dietrich, W.E., Leverich, G.T., Sklar, L.S., 2009. Experimental evidence for the conditions necessary to sustain meandering in coarse-bedded rivers. Proc. Natl. Acad. Sci. 106, 16936–16941. https://doi.org/10.1073/pnas.0909417106

Brice, J.C., 1973. Meandering pattern of the White River in Indiana: an analysis. In: Morisawa, M. (Ed.), Fluvial Geomorphology, Allen and Unwin, pp. 178-200.

Brice, J.C., 1974. Evolution of meander loops. Geological Society of America Bulletin 85, 581-586.

Brice, J.C., 1975. Airphoto interpretation of the form and behavior of alluvial rivers, Final report to the U.S Army Research Office-Durham. Washington University, St. Louis, p. 10.

Brice, J.C., 1982. Stream channel stability assessment (No. FHWA/RD-82-021). Federal Highway Administration, Office of Research and Development, p. 43.

Brice, J.C., 1984. Planform properties of meandering rivers, in: Elliott, C.M. (Ed.), River Meandering. American Society of Civil Engineers, pp. 1–15.

Burgess, P.M., Hovius, N., 1998. Rates of delta progradation during highstands: Consequences for timing of deposition in deep-marine systems. J. Geol. Soc. 155, 217–222. https://doi.org/10.1144/gsjgs.155.2.0217

Calder, B., 2006. On the uncertainty of archive hydrographic data sets. IEEE Journal of Oceanic Engineering 31, 249-265.

Calder, B., 2007. Multi-algorithm swath consistency detection for multibeam echosounder data. The International Hydrographic Review 8, 9-25.

Caley, T., Malaizé, B., Revel, M., Ducassou, E., Wainer, K., Ibrahim, M., Shoeaib, D., Migeon, S., Marieu, V., 2011. Orbital timing of the Indian, East Asian and African boreal monsoons and the concept of a “global monsoon.” Quat. Sci. Rev. 30, 3705–3715. https://doi.org/10.1016/j.quascirev.2011.09.015

Carter, L., Burnett, D., Drew, S., Marle, G., Hagadorn, L., Bartlett-McNeil, D., Irvine, N., 2009. Submarine cables and the Oceans – Connecting the world. UNEP -WCMC Biodiversity Series No. 31. ICPC/UNEP/UNEP-WCMC

Clark, J.D., Pickering, K.T., 1996. Submarine Channels- Processes and Architecture. Vallis Press London, p.231.

Clark, J., Kenyon, N., Pickering, K., 1992. Quantitative analysis of the geometry of submarine levees. Geology 60, 877–910. https://doi.org/10.1130/0091-7613(1992)020<0633

Constantine, J.A., Dunne, T., Ahmed, J., Legleiter, C., Lazarus, E.D., 2014. Sediment supply as a driver of river meandering and floodplain evolution in the Amazon Basin. Nature Geoscience 7, 899-903.

Corney, R.K.T., Peakall, J., Parsons, D.R., Elliott, L., Amos, K.J., Best, J.L., Keevil, G.M., Ingham, D.B., 2006. The orientation of helical flow in curved channels. Sedimentology 53, 249–257. https://doi.org/10.1111/j.1365-3091.2006.00771.x

Corney, R.K.T., Peakall, J., Parsons, D.R., Elliott, L., Best, J.L., Thomas, R.E., Keevil, G.M., Ingham, D.B., Amos, K.J., 2008. Reply to Discussion of Imran et al. on “The orientation of helical flow in curved channels” by Corney et al., Sedimentology, 53, 249-257. Sedimentology 55, 241–247. https://doi.org/10.1111/j.1365-3091.2007.00925.x

Cossu, R., Wells, M.G., 2013. The evolution of submarine channels under the influence of Coriolis forces: experimental observations of flow structures. Terra Nova 25, 65–71. https://doi.org/10.1111/ter.12006

Cossu, R., Wells, M.G., Peakall, J., 2015. Latitudinal variations in submarine channel sedimentation patterns: the role of Coriolis forces. J. Geol. Soc. 172, 161–174. https://doi.org/10.1144/jgs2014-043

Covault, J.A., Graham, S.A., 2010. Submarine fans at all sea-level stands: Tectono-morphologic and climatic controls on terrigenous sediment delivery to the deep sea. Geology 38, 939–942. https://doi.org/10.1130/G31081.1

Curray, J.R., Emmel, F.J., Moore, D.G., 2003. The Bengal Fan: morphology, geometry, stratigraphy, history and processes. Mar. Pet. Geol. 19, 1191–1223. https://doi.org/10.1016/S0264-8172(03)00035-7

Czuba, J.A., Best, J.L., Oberg, K.A., Parsons, D.R., Jackson, P.R., Garcia, M.H., Ashmore, P., 2011. Bed morphology, flow structure and sediment transport at the outlet of Lake Huron and in the upper St. Clair River. Journal of Great Lakes Research 37, 480-493.

Darby, S.E., Peakall, J., 2012. Modelling the equilibrium bed topography of submarine meanders that exhibit reversed secondary flows. Geomorphology 163–164, 99–109. https://doi.org/10.1016/j.geomorph.2011.04.050

Davarpanah Jazi, S., Wells, M.G., Peakall, J., Dorrell, R.M., Thomas, R.E., Keevil, G.M., Darby, S.E., Sommeria, J., Viboud, S., Valran, T., 2020. Influence of Coriolis force upon bottom boundary layers in a large-scale gravity current experiment:

Implications for evolution of sinuous deep-water channel systems. J. Geophys. Res. – Oceans 125, e2019JC015284. doi: 10.1029/2019JCO15284

de Ruig, M.J., 2003. Deep Marine sedimentation and gas reservoir distribution in upper Austria. Oil Gas Eur. Mag. 29, 64–73.

Deptuck, M.E., Sylvester, Z., Pirmez, C., O'Byrne, C., 2007. Migration–aggradation history and 3-D seismic geomorphology of submarine channels in the Pleistocene Benin-major Canyon, western Niger Delta slope. Mar. Pet. Geol. 24, 406–433. https://doi.org/10.1016/j.marpetgeo.2007.01.005

Dietrich, W.E., 1987. Mechanics of flow and sediment transport in river bends, in: Richards, K.S. (Ed.), River Channels. Blackwell, Oxford, pp. 179–227.

Donovan, M., Belmont, P., Sylvester, Z., 2021. Evaluating the relationship between meander-bend curvature, sediment supply, and migration rates. J. Geophys. Res. Earth Surf., doi: 10.1029/2020JF006058.

Dorrell, R.M., Darby, S.E., Peakall, J., Sumner, E.J., Parsons, D.R., Wynn, R.B., 2013. Superelevation and overspill control secondary flow dynamics in submarine channels. J. Geophys. Res. Oceans 118, 3895–3915. https://doi.org/10.1002/jgrc.20277

Dorrell, R.M., Peakall, J., Burns, C., Keevil, G.M., 2018. A novel mechanism in sinuous seafloor channels: Implications for submarine channel evolution. Geomorphology 303, 1-12.

Droz, L., Rigaut, F., Cochonat, P., Tofani, R., 1996. Morphology and recent evolution of the Zaire turbidite system (Gulf of Guinea). Geol. Soc. Am. Bull. 108, 253–269. https://doi.org/10.1130/0016-7606(1996)108<0253

Droz, L., Marsset, T., Ondréas, H., Lopez, M., Savoye, B., Spy-Anderson, F.L., 2003. Architecture of an active mud-rich turbidite system: The Zaire Fan (Congo-Angola margin southeast Atlantic): Results from ZaïAngo 1 and 2 cruises. Am. Assoc. Pet. Geol. Bull. 87, 1145–1168. https://doi.org/10.1306/03070300013

Duró, G., Crosato, A., Tassi, P., 2016. Numerical study on river bar response to spatial variations of channel width. Adv. Water Resour. 93, 21–38. https://doi.org/10.1016/j.advwatres.2015.10.003

Eke, E., Czapiga, M.J., Viparelli, E., Shimizu, Y., Imran, J., Sun, T., Parker, G., 2014a. Coevolution of width and sinuosity in meandering rivers. J. Fluid Mech. 760, 127–174. https://doi.org/10.1017/jfm.2014.556

Eke, E., Parker, G., Shimizu, Y., 2014b. Numerical modeling of erosional and depositional bank processes in migrating river bends with self-formed width: Morphodynamics of bar push and bank pull. J. Geophys. Res. Earth Surf. 119, 1455–1483. https://doi.org/10.1002/2013JF003020

Ezz, H., Imran, J., 2014. Curvature-induced secondary flow in submarine channels. Environ. Fluid Mech. 14, 343–370. https://doi.org/10.1007/s10652-014-9345-4

Flood, R.D., Damuth, J.E., 1987. Quantitative characteristics of sinuous distributary channels on the Amazon Deep-Sea Fan. Geol. Soc. Am. Bull. 98, 728–738. https://doi.org/10.1130/0016-7606(1987)98<728

Giorgio Serchi, F., Peakall, J., Ingham, D.B., Burns, A.D., 2011. A unifying computational fluid dynamics investigation on the river-like to river-reversed secondary circulation in submarine channel bends. J. Geophys. Res. 116, C06012. https://doi.org/10.1029/2010JC006361

Guiastrennec-Faugas, L., Gillet, H., Silva Jacinto, R., Dennielou, B., Hanquiez, V., Schmidt, S., Simplet, L., Rousset, A., 2020. Upstream migrating knickpoints and related sedimentary processes in a submarine canyon from a rare 20-year morphobathymetric time-lapse (Capbreton submarine canyon, Bay of Biscay, France). Mar. Geol. 423, 106143. https://doi.org/10.1016/j.margeo.2020.106143

Guiastrennec-Faugas, L., Gillet, H., Peakall, J., Dennielou, B., Gaillot, A., Silva Jacinto, R., 2021. Initiation and evolution of knickpoints and their role in cut-and-fill processes in active submarine channels. Geology 49, 314-319, https://doi.org/10.1130/G48369.1

Heijnen, M.S., Clare, M.A., Cartigny, M.J.B., Talling, P.J., Hage, S. Lintern, D.G., Stacey, C., Parsons, D.R., Simmons, S.M., Sumner, E.J., Dix, J.K. , Hughes Clarke, J.E., 2020. Rapidly-migrating and internally-generated knickpoints can control submarine channel evolution. Nat. Commun. 11, 3129. https://doi.org/10.1038/s41467-020-16861-x

Hansen, L.A.S., Callow, R.H.T., Kane, I.A., Gamberi, F., Rovere, M., Cronin, B.T., Kneller, B.C., 2015. Genesis and character of thin-bedded turbidites associated with submarine channels. Mar. Pet. Geol. 67, 852–879. https://doi.org/10.1016/j.marpetgeo.2015.06.007

Heezen, B.C., Menzies, R.J., Schneider, E.D., Ewing, W.M., Granelli, N.C.I., 1964. Congo submarine canyon. Am. Assoc. Pet. Geol. Bull. 48, 1126–1149. https://doi.org/10.1306/83D9102E-16C7-11D7-8645000102C1865D

Hodgson, D.M., Di Celma, C.N., Brunt, R.L., Flint, S.S., 2011. Submarine slope degradation and aggradation and the stratigraphic evolution of channel-levee systems. J. Geol. Soc. 168, 625–628. https://doi.org/10.1144/0016-76492010-177

Hooke, J.M., 2007. Complexity, self-organisation and variation in behaviour in meandering rivers. Geomorphology 91, 236–258. https://doi.org/10.1016/j.geomorph.2007.04.021

Hudson, P.F., 2002. Pool-Riffle morphology in an actively migrating alluvial channel: the Lower Mississippi River. Phys. Geogr. 23, 154–169. https://doi.org/10.2747/0272-3646.23.2.154

Imran, J., Parker, G., Pirmez, C., 1999. A nonlinear model of flow in meandering submarine and subaerial channels. J. Fluid Mech. 400, 295–331. https://doi.org/10.1017/S0022112099006515

Islam, M.A., Imran, J., Pirmez, C., Cantelli, A., 2008. Flow splitting modifies the helical motion in submarine channels. Geophys. Res. Lett. 35, L22603.

Janocko, M., Cartigny, M.B.J., Nemec, W., Hansen, E.W.M., 2013. Turbidity current hydraulics and sediment deposition in erodible sinuous channels: Laboratory experiments and numerical simulations. Mar. Pet. Geol. 41, 222–249. https://doi.org/10.1016/j.marpetgeo.2012.08.012

Jansen, J.H.F., Giresse, P., Moguedet, G., 1984. Structural and sedimentary geology of the Congo and Southern Gabon continental shelf; a seismic and acoustic reflection survey. Neth. J. Sea Res. 17, 364–384. https://doi.org/10.1016/0077-7579(84)90056-5

Jobe, Z.R., Howes, N.C., Auchter, N.C., 2016. Comparing submarine and fluvial channel kinematics: Implications for stratigraphic architecture. Geology 44, 931–934. https://doi.org/10.1130/G38158.1

Jobe, Z.R., Howes, N.C., Straub, K.M., Cai, D., Deng, H., Laugier, F.J., Pettinga, L.A., Shumaker, L.E., 2020. Comparing aggradation, superelevation, and avulsion frequency of submarine and fluvial channels. Front. Earth Sci. 8. https://doi.org/10.3389/feart.2020.00053

Kane, I.A., Hodgson, D.M., 2011. Sedimentological criteria to differentiate submarine channel levee subenvironments: Exhumed examples from the Rosario Fm. (Upper Cretaceous) of Baja California, Mexico, and the Fort Brown Fm. (Permian), Karoo Basin, S. Africa. Mar. Pet. Geol. 28, 807–823. https://doi.org/10.1016/j.marpetgeo.2010.05.009

Keevil, G.M., Peakall, J., Best, J.L., Amos, K.J., 2006. Flow structure in sinuous submarine channels: Velocity and turbulence structure of an experimental submarine channel. Mar. Geol. 229, 241–257. https://doi.org/10.1016/j.margeo.2006.03.010

Keevil, G.M., Peakall, J., Best, J.L., 2007. The influence of scale, slope and channel geometry on the flow dynamics of submarine channels. Mar. Pet. Geol. 24, 487–503. https://doi.org/10.1016/j.marpetgeo.2007.01.009

Keller, E.A., Melhorn, W.N., 1978. Rhythmic spacing and origin of pools and riffles: discussion. Geol. Soc. Am. Bull. 89, 723–730. https://doi.org/10.1130/0016-7606(1980)91<248:rsaoop>2.0.co;2

Khripounoff, A., Vangriesheim, A., Babonneau, N., Crassous, P., Dennielou, B., Savoye, B., 2003. Direct observation of intense turbidity current activity in the Zaire submarine valley at 400 m water depth. Mar. Geol. 194, 151–158. https://doi.org/10.1016/S0025-3227(02)00677-1

Klaucke, I., Hesse, R., Ryan, W.B.F., 1997. Flow parameters of turbidity currents in a low-sinuosity giant deep-sea channel. Sedimentology 44, 1093–1102. https://doi.org/10.1111/j.1365-3091.1997.tb02180.x

Knighton, A.D., 1982. Asymmetry of river channel cross-sections: Part II. mode of development and local variation. Earth Surf. Process. Landf. 7, 117–131. https://doi.org/10.1002/esp.3290070206

Kolla, V., 2007. A review of sinuous channel avulsion patterns in some major deep-sea fans and factors controlling them. Mar. Pet. Geol. 24, 450–469. https://doi.org/10.1016/j.marpetgeo.2007.01.004

Kolla, V., Coumes, F., 1987. Morphology, internal structure, seismic stratigraphy, and sedimentation of Indus Fan. Am. Assoc. Pet. Geol. Bull. 71, 650-677.

Konsoer, K., Zinger, J., Parker, G., 2013. Bankfull hydraulic geometry of submarine channels created by turbidity currents: Relations between bankfull channel characteristics and formative flow discharge. J. Geophys. Res. Earth Surf. 118, 216–228. https://doi.org/10.1029/2012JF002422

Kudrass, H.R., Michels, K.H., Wiedicke, M., Suckow, A., 1998. Cyclones and tides as feeders of a submarine canyon off Bangladesh. Geology 26, 715–718. https://doi.org/10.1130/0091-7613(1998)026<0715:CATAFO>2.3.CO;2

Lagasse, P.F., Spitz, W.J., Zevenberger, L.W., Zachmann, D.W., 2004. Handbook for predicting stream meander migration. National Cooperative Highway Research Program.

Laurent, D., Marsset, T., Droz, L., Granjeon, D., Molliex, S., Picot, M., Rabineau, M., 2020. 4D forward stratigraphic modelling of the Late Quaternary Congo deep-sea fan: Role of climate/vegetation coupling in architectural evolution. Marine Geology 429, 106334. https://doi.org/10.1016/j.margeo.2020.106334

Lemay, M., Grimaud, J.-L., Cojan, I., Rivoirard, J., Ors, F., 2020. Geomorphic variability of submarine channelized systems along continental margins: Comparison with fluvial meandering channels. Mar. Pet. Geol. 115, 104295.

Leopold, L.B., 1982. Water surface topography in river channels and implications for meander development, in: Hey, R.D., Bathurst, J.C. and Wiley, T. (Eds.), Gravel-Bed Rivers, John Wiley, pp. 359-383.

Leopold, L.B., Wolman, M.G., 1960. River meanders. Geol. Soc. Am. Bull. 71, 769–793. https://doi.org/10.1130/0016-7606(1960)71

Luchi, R., Bolla Pittaluga, M., Seminara, G., 2012. Spatial width oscillations in meandering rivers at equilibrium. Water Resour. Res. 48, W05551. https://doi.org/10.1029/2011WR011117

Maier, K.L., Fildani, A., Paull, C.K., McHargue, T.R., Graham, S.A., Caress, D.W., 2013. Deep-sea channel evolution and stratigraphic architecture from inception to abandonment from high-resolution Autonomous Underwater Vehicle surveys offshore central California. Sedimentology 60, 935–960. https://doi.org/10.1111/j.1365-3091.2012.01371.x

Marsset, T., Droz, L., Dennielou, B., Pichon, E., 2009. Cycles in the architecture of the Quaternary Zaire Turbidite System: a possible link with climate. In: Kneller, B., Martinsen, O.J. and McCaffrey, B. External Controls on Deep-Water Depositional Systems, Soc. Sediment. Geol. Spec. Publ. 92, 89–106. https://doi.org/10.2110/sepmsp.092.089

Matsubara, Y., Howard, A.D., 2014. Modeling planform evolution of a mud-dominated meandering river: Quinn River, Nevada, USA. Earth Surf. Process. Landf. 39, 1365–1377. https://doi.org/10.1002/esp.3588

Mayall, M., Jones, E., Casey, M., 2006. Turbidite channel reservoirs—Key elements in facies prediction and effective development. Mar. Pet. Geol. 23, 821–841. https://doi.org/10.1016/j.marpetgeo.2006.08.001

Micheli, E.R., Larse, E.W., 2010. River channel cutoff dynamics, Sacramento River, California, USA. River Res. Appl. 27, 328–344. https://doi.org/10.1002/rra

Migeon, S., Savoye, B., Babonneau, N., Spy-Andersson, F.-L., 2004. Processes of sediment-wave construction along the present Zaire deep-sea meandering channel: Role of meanders and flow stripping. J. Sediment. Res. 74, 580–598. https://doi.org/10.1306/091603740580

Morris, E.A., Hodgson, D.M., Brunt, R.L., Flint, S.S., 2014a. Origin, evolution and anatomy of silt-prone submarine external levées. Sedimentology 61, 1734–1763. https://doi.org/10.1111/sed.12114

Morris, E.A., Hodgson, D.M., Flint, S.S., Brunt, R.L., Butterworth, P.J., Verhaeghe, J., 2014b. Sedimentology, stratigraphic architecture, and depositional context of submarine frontal-lobe complexes. J. Sediment. Res. 84, 763–780. https://doi.org/10.2110/jsr.2014.61

Nakajima, T., Satoh, M., Okamura, Y., 1998. Channel-levee complexes, terminal deep-sea fan and sediment wave fields associated with the Toyama Deep-Sea Channel system in the Japan Sea. Mar. Geol. 147, 25–41. https://doi.org/10.1016/S0025-3227(97)00137-0

Nakajima, T., Peakall, J., McCaffrey, W.D., Paton, D.A., Thompson, P.J.P., 2009. Outer-Bank Bars: A new intra-channel architectural element within sinuous submarine slope channels. J. Sediment. Res. 79, 872–886. https://doi.org/10.2110/jsr.2009.094

Nanson, G.C., 1980. Point bar and floodplain formation of the meandering Beatton River, northeastern British Columbia, Canada. Sedimentology 27, 3–29. https://doi.org/10.1111/j.1365-3091.1980.tb01155.x

Nanson, G.C., Hickin, E.J., 1983. Channel migration and incision on the Beatton River. J. Hydraul. Eng. 109, 327–337. https://doi.org/10.1061/(ASCE)0733-9429(1983)109:3(327)

Nelson, J.M., Smith, J.D., 1989. Evolution and stability of erodible channel beds, in: Ikeda, S., Parker, G. (Eds.), River Meandering. American Geophysical Union, pp. 321–377. https://doi.org/10.1029/wm012p0321

Page, K.J., Nanson, G.C., Frazier, P.S., 2003. Floodplain formation and sediment stratigraphy resulting from oblique accretion on the Murrumbidgee River, Australia. J. Sediment. Res. 73, 5–14. https://doi.org/10.1306/070102730005

Parker, G., Shimizu, Y., Wilkerson, G.V., Eke, E.C., Abad, J.D., Lauer, J.W., Paola, C., Dietrich, W.E., Voller, V.R., 2011. A new framework for modeling the migration of meandering rivers. Earth Surf. Process. Landf. 36, 70–86. https://doi.org/10.1002/esp.2113

Peakall, J., Sumner, E.J., 2015. Submarine channel flow processes and deposits: a process-product perspective. Geomorphology 244, 95–120. https://doi.org/10.1016/j.geomorph.2015.03.005

Peakall, J., McCaffrey, B., Kneller, B., 2000a. A process model for the evolution, morphology, and architecture of sinuous submarine channels. J. Sediment. Res. 70, 434–448. https://doi.org/10.1306/2dc4091c-0e47-11d7-8643000102c1865d

Peakall, J., McCaffrey, W.D., Kneller, B.C., Stelting, C.E., McHargue, T.R., Schweller, W.J., 2000b. A process model for the evolution of submarine fan channels: Implications for sedimentary architecture, in: Bouma, A.H., Stone, C.G. (Eds.), Fine-Grained Turbidite Systems. AAPG Memoir 72 /SEPM Special Publication 68, pp. 73–87.

Peakall, J., Amos, K.J., Keevil, G.M., Bradbury, P.W., Gupta, S., 2007. Flow processes and sedimentation in submarine channel bends. Mar. Pet. Geol. 24, 470–486. https://doi.org/10.1016/j.marpetgeo.2007.01.008

Pickering, K.T., Hiscott, R.N., 2015. Deep Marine Systems: Processes, Deposits, Environments, Tectonics and Sedimentation. American Geophysical Union, p.672.

Picot, M., Droz, L., Marsset, T., Dennielou, B., Bez, M., 2016. Controls on turbidite sedimentation: Insights from a quantitative approach of submarine channel and lobe architecture (Late Quaternary Congo Fan). Mar. Pet. Geol. 72, 423–446. https://doi.org/10.1016/j.marpetgeo.2016.02.004

Picot, M., Marsset, T., Droz, L., Dennielou, B., Baudin, F., Hermoso, M., de Rafelis, M., Sionneau, T., Cremer, M., Laurent, D., Bez, M., 2019. Monsoon control on channel avulsions in the Late Quaternary Congo Fan. Quat. Sci. Rev. 204, 149–171. https://doi.org/10.1016/j.quascirev.2018.11.033

Pirmez, C., Imran, J., 2003. Reconstruction of turbidity currents in Amazon Channel. Mar. Pet. Geol. 20, 823–849. https://doi.org/10.1016/j.marpetgeo.2003.03.005

Pope, E.L., Talling, P., Carter, L. 2017. Which earthquakes trigger damaging submarine mass movements: Insights from a global record of submarine cable breaks? Mar. Geol. 384, 131-146. https://doi.org/10.1016/j.margeo.2016.01.009

Posamentier, H.W., 2003. Depositional elements associated with a basin floor channel-levee system : case study from the Gulf of Mexico. Mar. Petr. Geol. 20, 677–690. https://doi.org/10.1016/j.marpetgeo.2003.01.002

Prélat, A., Covault, J.A., Hodgson, D.M., Fildani, A., Flint, S.S., 2010. Intrinsic controls on the range of volumes, morphologies, and dimensions of submarine lobes. Sediment. Geol. 232, 66–76. https://doi.org/10.1016/j.sedgeo.2010.09.010

Reimchen, A.P., Hubbard, S.M., Stright, L., Romans, B.W., 2016. Using sea-floor morphometrics to constrain stratigraphic models of sinuous submarine channel systems. Mar. Pet. Geol. 77, 92–115. https://doi.org/10.1016/j.marpetgeo.2016.06.003

Rossi, C.E., 2012. Developing hydraulic relationships at the riffle crest thalweg in gravel bed streams (Master of Science). Humboldt State University.

Russell, C.E., 2017. Prediction of sedimentary architecture and lithological heterogeneity in fluvial point-bar deposits (PhD thesis). University of Leeds.

Russell, C.E., Mountney, N.P., Hodgson, D.M., Colombera, L., 2019. A novel approach for prediction of lithological heterogeneity in fluvial point-bar deposits from analysis of meander morphology and scroll-bar pattern, in: Ghinassi, M., Colombera, L., Mountney, N.P., Reesink, A.J.H., Bateman, M. (Eds.), Fluvial Meanders and Their Sedimentary Products in the Rock Record. John Wiley & Sons, Ltd, Chichester, UK, pp. 385–417. https://doi.org/10.1002/9781119424437.ch15

Savoye, B., Babonneau, N., Dennielou, B., Bez, M., 2009. Geological overview of the Angola–Congo margin, the Congo deep-sea fan and its submarine valleys. Deep Sea Res. Part II Top. Stud. Oceanogr. 56, 2169–2182. https://doi.org/10.1016/j.dsr2.2009.04.001

Schwenk, T., Spieß, V., Breitzke, M., Hübscher, C., 2005. The architecture and evolution of the Middle Bengal Fan in vicinity of the active channel-levee system imaged by high-resolution seismic data. Mar. Pet. Geol. 22, 637–656. https://doi.org/10.1016/j.marpetgeo.2005.01.007

Seminara, G., Tubino, M., 1989. Alternate bars and meandering: free, forced and mixed interactions. Water Resour. Manag. 12, 267–320. https://doi.org/10.1029/wm012p0267

Shumaker, L.E., Jobe, Z.R., Johnstone, S.A., Pettinga, L.A., Cai, D., Moody, J.D., 2018. Controls on submarine channel-modifying processes identified through morphometric scaling relationships. Geosphere 14, 2171–2187. https://doi.org/10.1130/GES01674.1

Straub, K.M., Mohrig, D., McElroy, B., Buttles, J., Pirmez, C., 2008. Interactions between turbidity currents and topography in aggrading sinuous submarine channels: a laboratory study. Geol. Soc. Am. Bull. 120, 368–385. https://doi.org/10.1130/B25983.1

Straub, K.M., Mohrig, D., Buttles, J., McElroy, B., Pirmez, C., 2011a. Quantifying the influence of channel sinuosity on the depositional mechanics of channelized turbidity currents: A laboratory study. Mar. Pet. Geol. 28, 744–760.

Straub, K.M., Mohrig, D., Pirmez, C., 2011b. Architecture of an aggradational tributary submarine-channel network on the continental slope offshore Brunei Darussalam. Appl. Princ. Seism. Geomorphol. Cont.-Slope Base--Slope Syst. Case Stud. Seafloor -Seafloor Analog. 99, 13–30. https://doi.org/10.1029/2008JF001190

Sylvester, Z., Pirmez, C., Cantelli, A., 2011. A model of submarine channel-levee evolution based on channel trajectories: Implications for stratigraphic architecture. Mar. Pet. Geol. 28, 716–727. https://doi.org/10.1016/j.marpetgeo.2010.05.012

Tinkler, K.J., 1970. Pools, riffles, and meanders. Geol. Soc. Am. Bull. 81, 547–552. https://doi.org/10.1130/0016-7606(1970)81[547:PRAM]2.0.CO;2

Trush, W.J., McBain, S.M, Leopold, L.B. 2000. Attributes of an alluvial river and their relation to water policy and management. PNAS 97, 11858–11863. https://doi.org/10.1073/pnas.97.22.11858

van de Lageweg, W.I., Van Dijk, W.M., Baar, A.W., Rutten, J., Kleinhans, M.G., 2014. Bank pull or bar push: What drives scroll-bar formation in meandering rivers? Geology 42, 319–322. https://doi.org/10.1130/G35192.1

van den Berg, J.H., 1995. Prediction of alluvial channel pattern of perennial rivers. Geomorphology 12, 259–279. https://doi.org/10.1016/0169-555X(95)00014-V

van Weering, T.C.E., van Iperen, J., 1984. Fine-grained sediments of the Zaire deep-sea fan, southern Atlantic Ocean. In: D.A.V. Stow and D.J.W. Piper (Eds.), Fine-grained Sediments: Deep-water Processes and Facies. Geol. Soc. London Spec. Publ. 15, 95–113. https://doi.org/10.1144/GSL.SP.1984.015.01.06

Vangriesheim, A., Khripounoff, A., Crassous, P., 2009. Deep-Sea Research II Turbidity events observed in situ along the Congo submarine channel. Deep-Sea Res. Part II 56, 2208–2222. https://doi.org/10.1016/j.dsr2.2009.04.004

Vendettuoli, D., Clare, M.A., Clarke, J.E.H., Vellinga, A., Hizzett, J., Hage, S., Cartigny, M.J.B., Talling, P.J., Waltham, D., Hubbard, S.M., Stacey, C., Lintern, D.G.,

2019. Daily bathymetric surveys document how stratigraphy is built and its extreme incompleteness in submarine channels. Earth Planet. Sci. Lett. 515, 231-247, 10.1016/J.EPSL.2019.03.033

Weisstein, E.W., 2021. Square point picking. From *MathWorld* - A Wolfram web resource, https://mathworld.wolfram.com/SquarePointPicking.html

Wells, M., Cossu, R., 2013. The possible role of Coriolis forces in structuring large-scale sinuous patterns of submarine channel-levee systems. Philos. Trans. R. Soc. A. 371, 20120366. https://doi.org/10.1098/rsta.2012.0366

Wells, M.G., Dorrell, R.M., 2021. Turbulence processes within turbidity currents. Annu. Rev. Fluid Mech. 53, 59-83.

Wetzel, A., 1993. The transfer of river load to deep-sea fans: a quantitative approach. Am. Assoc. Pet. Geol. Bull. 77, 1679–1692. https://doi.org/10.1306/BDFF8EFC-1718-11D7-8645000102C1865D

Wu, C., Ullah, M.S., Lu, J., Bhattacharya, J.P., 2016. Formation of point bars through rising and falling flood stages: Evidence from bar morphology, sediment transport and bed shear stress. Sedimentology 63, 1458–1473. https://doi.org/10.1111/sed.12269

Wynn, R.B., Stow, D.A.V., 2002. Classification and characterisation of deep-water sediment waves. Mar. Geol. 192, 7–22. https://doi.org/10.1016/S0025-3227(02)00547-9

Wynn, R.B., Cronin, B.T., Peakall, J., 2007. Sinuous deep-water channels: Genesis, geometry and architecture. Mar. Pet. Geol. 24, 341–387. https://doi.org/10.1016/j.marpetgeo.2007.06.001

Zhou, J., Chang, H.H., Stow, D., 1993. A model for phase lag of secondary flow in river meanders. J. Hydrol. 146, 73–88. https://doi.org/10.1016/0022-1694(93)90270-J

Zolezzi, G., Luchi, R., Tubino, M., 2012. Modeling morphodynamic processes in meandering rivers with spatial width variations. Rev. Geophys. 50, 1–24. https://doi.org/10.1029/2012RG000392